NTNU – Trondheim
Norwegian University of
Science and Technology

Deposition of Thin Film Electrolyte by Pulsed Laser Deposition (PLD) for micro-SOFC Development

Hedda Nordby Krogstad

Materials Science and Engineering
Submission date: June 2012
Supervisor: Paul Inge Dahl, IMTE

Norwegian University of Science and Technology
Department of Materials Science and Engineering

Abstract

Yttria Stabilized Zirconia (YSZ) have been deposited on silicon-based chips (1x1 cm) by Pulsed Laser Deposition (PLD) under varying conditions. The purpose was to identify the optimal deposition parameters to obtain a YSZ thin-film with a dense, crystalline, and columnar structure for micro-SOFC electrolyte applications. The deposition temperature was held constant, at 600 C°, while the deposition oxygen pressure, P_{O_2}, and the target-substrate distance (referred to as WD, i.e. working distance) were systematically changed from 20 to 150 mTorr and from 90 to 130 mm, respectively. The amount of laser pulses was 40 000 in all deposits, except from one sample that was deposited with 80 000 laser pulses to study the influence of film thickness.

Both film thickness and film density decreased with increasing P_{O_2}. The thickness of the deposited films ranged from 15 to 239 nm, and it was found that the thickness decreased linearly with increasing WD and exponentially with increasing P_{O_2}.

Below 50 mTorr, a tendency towards densification of the columnar structure was identified. This was due to a high kinetic energy (and thus significant surface diffusion) of the ablated species at the substrate surface. A dense, crystalline film composed of columnar grains was achieved by depositing YSZ in a P_{O_2} of 20 mTorr. The WD did not show any great influence on microstructure and density.

The orientation of the YSZ films were found to vary as a function of P_{O_2} and film thickness. A clear tendency towards a (111) orientation was identified from 50 mTorr and below. Above 50 mTorr, a (200) orientation was found to dominate with increasing film thickness, and was associated with the introduction of porosity in the film due to shadowing effects. The thickest samples (deposited at the lowest P_{O_2} and shortest WD) showed a tendency towards developing a grain orientation distribution similar to that of bulk-YSZ.

Deposition of YSZ on silicon-based wafers (10 cm in diameter) was performed with a following analysis of film thickness homogeneity. Mirror rastering was applied with different velocity patterns, and it was found that exponentially increasing the raster velocity from the edge of the wafer towards the center improves film thickness homogeneity.

Preface

The master thesis here presented was carried out as an external master from NTNU at the "Catalonia Institute for Energy Research" (IREC) in Barcelona, Spain. The host group for the thesis was "Nanoionics and Fuel Cells" (lead by Dr. Albert Tarancón), which is a sub-group in the field of "Advanced Materials for Energy" lead by Prof. Dr. Joan Ramón Morante. This specific thesis was realized as a part of an ongoing project on micro-Solid Oxide Fuel Cells (micro-SOFC's) at IREC, where researchers are cooperating to obtain a complete micro-SOFC device. The motivation for this thesis was up-scaling of the manufacturing process of a single fuel cell unit, as a step towards industrial production of micro-SOFC by enabling deposition of electrolyte material on large-area substrates.

Supervision and guidance was provided by Dr. Albert Tarancón (IREC) and Paul Inge Dahl (SINTEF and NTNU). I wish to thank all of my fellow colleagues at IREC, Doris Pla and Saranya Aruppukottai for all help and kindness, and to Albert Tarancón for great guidance and expertise, and for answering so positively on my request to perform a master thesis at IREC, and making it reality. I also wish to thank Emma Rosinyol for so kindly contributing to the realization of both TEM sample preparation and TEM analysis. An extra thanks to Alex Morata, for patience, kindness, training on all equipment and for sharing frustrations and enthusiasm. A special thanks to Iñigo Garbayo for all his knowledge and enlightening, as well as for good discussions and laughs. At last, thanks to Paul Inge Dahl, even if you were more than 3000 km away, your encouragement and knowledge has been to great help.

Contents

List of Figures

List of Tables

Introduction

Micro-SOFCs are promising power sources for portable electronic devices due to their high energy conversion efficiency, large energy density and the capability of operating on different fuels [1]. A micro-SOFC differs from a conventional SOFC in size, with lateral dimensions down to sub-micrometers for key components such as the electrolyte membrane. The smaller dimension result in decreased ohmic losses which are linearly dependent on the electrolyte thickness, i.e. the diffusion length of the oxygen ions [2]. This allows to lower the operation temperature of the fuel cell to below $600^{\circ}C$, diminishing the well known problems related to material stability and compatibility in conventional SOFCs, which typically operate at temperatures around $1000^{\circ}C$ [2].

To produce an electrolyte in the sub-micrometer range, thin film deposition techniques such as Pulsed Laser Deposition (PLD) are required [2]. The thin-film is deposited onto a substrate material which is removed in subsequent processing steps, to achieve a free-standing electrolyte membrane. The basic idea of the PLD technique is ablation of a target material by rapid heating and evaporation of a small volume in the surface of the target using a pulsed, focused laser beam. Due to the pressure gradient the evaporated material is ejected towards the substrate, where it deposits by condensation [3]. The microstructure of the as-deposited thin-film is highly influenced by deposition parameters. Dense, crystalline films of YSZ with a columnar structure desired for micro-SOFC electrolyte applications are produced by carefully tuning deposition parameters such as PO_2, substrate temperature and WD.

There exist models predicting the influence of substrate temperature and gas pressure on as-deposited thin-film microstructure for physical vapor deposition techniques such as PLD [4]. A tendency towards higher film density is associated with both increasing temperature and decreasing pressure for deposition of YSZ, as a results of increased mobility of the deposited species [4]. It is however highlighted that results are not necessarily reproducible from one deposition technique to another, nor in two distinct devices of the same technique [2].

The PLD technique has been effectively limited to deposition onto small substrates [4]. Large area PLD now allows to deposit material onto substrates measuring up to 8 inches in diameter thanks the development of a mirror rastering system enabling movement of the pulsed laser beam across the target [5]. This again makes it possible to scale-up the production of thin-film electrolyte membranes, as a step towards industrialization of the production of micro-SOFC. However, a great challenge when depositing on large area substrates is to achieve complete film-thickness homogeneity [6]. Optimizing the rastering velocity as a function of plume position on the substrate is crucial, to avoid depositing more material in the center of the substrate than in the extremes.

The motivation of this project was to identify the optimal P_{O_2} and WD during deposition by the PLD technique for achieving YSZ thin-films with properties meeting the required criteria for micro-SOFC electrolyte applications. Another part of the project was dedicated to identifying the rastering conditions that yield a reasonable film-thickness homogeneity on large area substrates.

1 Theoretical background

To provide the reader with the theoretical background necessary to comprehend the motivation and discussion of this project, the first sections are dedicated to a thorough introduction to SOFCs and micro-SOFCs, as well as to the PLD technique and the state of the art electrolyte material, YSZ.

1.1 General principles of Solid Oxide Fuel Cells (SOFCs)

SOFCs convert chemical potential energy (in the form of a fuel and oxidizer species) directly into electrical energy [7]. Because there are no intermediate reaction products, a higher conversion coefficient is achieved compared to more conventional methods such as power production by steam turbines. Typical energy conversion efficiency in SOFCs is above 50% [8].

The active electrochemical element in a convetional SOFC is a three layer structure consisting of two porous electrodes separated by a dense, oxygen ion-conducting electrolyte [8]. The driving force for a SOFC is a differential P_{O_2} across the electrolyte [2]. At the cathode (high P_{O_2}), oxygen is reduced to O^{2-}, see Eq. 1.1, while at the anode (low P_{O_2}), oxidation of hydrogen or hydrocarbons leads to the formation of water (and CO_2 if the fuel carries hydrocarbons), see Eq. 1.2. An internal flux of oxygen ions across the electrolyte is balanced by an electrical current in an external load, yielding the total chemical reaction in Eq. 1.3. A figurative explanation of the basic principles of a SOFC can be seen i Fig. 1.

$$Cathode\ reaction : 1/2O_2(g) + 2e^- \rightarrow O^{2-} \tag{1.1}$$

$$Anode\ reaction : O^{2-} + H_2 \rightarrow H_2O + 2e^- \tag{1.2}$$

$$Total\ cell\ reaction : 1/2O_2 + H_2 \rightarrow H_2O \tag{1.3}$$

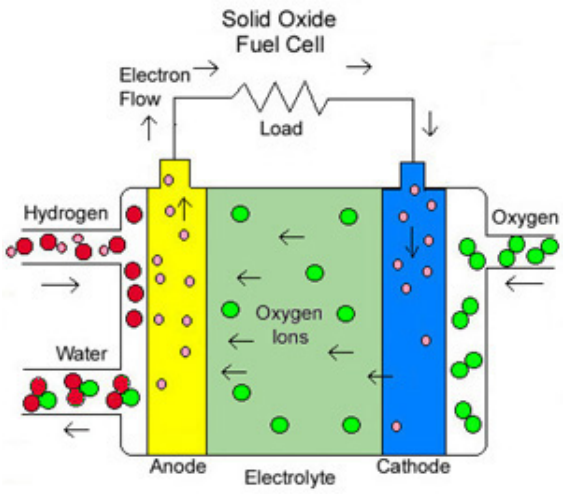

Figure 1: *Basic principles of a SOFC [9].*

The Nernst equation corresponding to the reaction defined in Eq. 1.3 can be expressed as

$$E = E^0 - \frac{RT}{2F} ln \frac{P_{H_2} P_{O_2}^{1/2}}{P_{H_2O}} \tag{1.4}$$

where R is the gas constant, T is the temperature of operation (Kelvin) and F is Faraday's constant. E^0 is the standard equilibrium voltage for the standard pressure (1 atm) at operating tempearture, i.e:

$$E^0(T) = \frac{\Delta G^0(T)}{2F} \tag{1.5}$$

where ΔG^0 is the Gibbs free energy variation of Eq. 1.3. At standard conditions, ΔG^0 in Eq. 1.5 amounts to 228.67 kJmol^{-1} when water is not condensed in the reaction. Putting this value into Eq. 1.4 yields a cell voltage of E = 1.185 V. This is the highest open cell voltage a conventional SOFC can achieve [8]. However, due to energy losses at the electrodes (cathode and anode activation and concentration polarization) and in the electrolyte (ohmic losses), the actual operating potential will be lower, and it will vary as a function of what chemical reaction is the limiting step [8]. An overview can be seen in Fig.2.

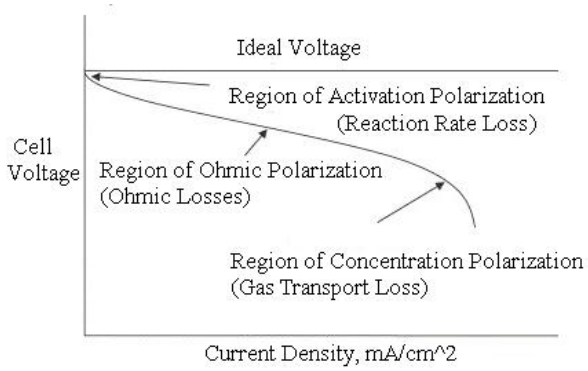

Figure 2: *Ideal and actual cellvoltage in a SOFC, the limiting reactions are indicated.*

The operating temperature of conventional SOFCs is relatively high (800-1000°C [2]). Such high temperatures are required because the ionic conductivity across the electrolyte (often >10 μm thick) is a thermally activated process and depends exponentially on temperature [7]. As a consequence of high operating temperatures, a slow start up and shut down of the cell is inevitable, and stringent criteria (mechanical, thermal and chemical stability) are put on all cell-component materials, which are some of the most significant disadvantages of conventional SOFCs. Lowering the operating temperatures would yield higher ohmic losses, as the resistivity of the electrolyte increases with decreasing temperature. The resistance, resulting in ohmic losses, is however a simple function of path length, meaning that a thinner electrolyte allows for lower operation temperatures without decreasing the power output of the fuel cell [8]. With electrolytes in the sub-micron scale, operating temperatures can be reduced to below 600°C, and down to 350°C [2]. For this, very different fabrication techniques and processing is required, and the fuel cell is referred to as a micro-SOFC.

1.2 Micro-SOFCs

Micro-SOFCs is based on the same principles as a conventional SOFCs, but the lateral dimensions are in the millimeter and sub-millimeter range. The reduction of the electrolyte thickness down to the nanometer-range allows for lower operation temperatures, as previously explained. This subsequently lowers the thermal response time and energy consumption during warm-up and cycling, as well as the material reactivity, resulting in a greater flexibility in the choice of materials [10]. There exist no standard for the ideal dimensions of the electrolyte, but literature states that below 300 nm further reduction of the electrolyte has little purpose, as current constrictions close to the electrochemically active area, i.e. the three-phase boundary, impedes further reduction of the resistivity [11] [2]. In general, an upper limit of 0.15 Ω/cm^2 area specif resistance (at desired operation temperature) is considered as the target value in micro-SOFC, thus the thickness of the electrolyte should be sufficiently thin to fulfill this requirement [10].

The power output of a single micro-SOFC is very dependent on design and processing techniques, but a value as high as 677 mW/cm^2 at 400°C is reported in literature [2]. By incorporating several single cells in a stack, the power range of a micro-SOFC systems is in the size of 1-20 watts. Combined with the small dimensions, micro-SOFCs are thus very appropriate for portable goods such as mobile phones and laptops [2]. In Fig.3 one can observe the superior performance of a micro-SOFC when comparing specific energy and energy density for many portable energy delivering devices such as conventional batteries [12]. This indicates that micro-SOFCs are smaller and lighter than other portable energy carriers, meaning it is possible to produce micro-SOFCs that provide a higher power output with the same dimensions as todays lithium-ion batteries, or provide a weight-and dimension reduction without decreasing the power output. It is predicted that micro-SOFC will achieve 3-4 times higher energy density than traditional Ni-metal hydride and Li-ion batteries [8].

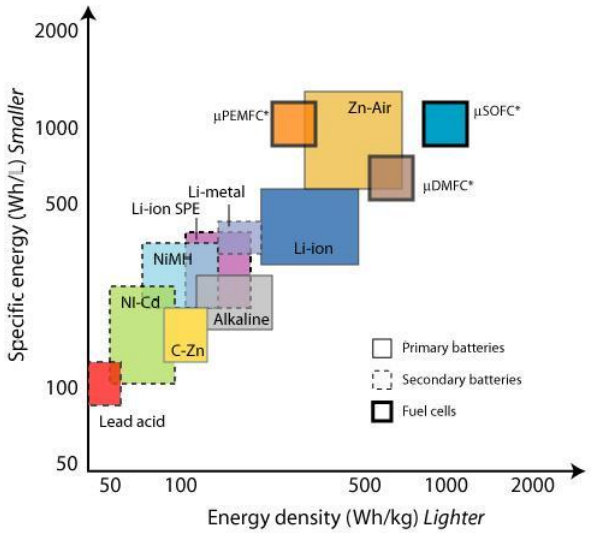

Figure 3: *Specific energy (per volume of device) and energy density (per mass of device) of several portable energy sources [12].*

1.2.1 Fabrication of micro-SOFCs

A large electrolyte area is desired in micro-SOFCs, because the overall performance is directly related to the electrochemically active area in each unit cell [2]. However, the mechanical stability of large area thin-films is poor, as critical stress to failure increase in proportion to $(h/r)^2$ where h is the thickness of the membrane, and r is the radius of the active membrane area [13]. Besides, thin-films are sensitive to defects such as pinholes (holes or reduced local thickness residing from shadowing effects during deposition), also favoring thicker films. In addition, thin-film depositions techniques such as PLD are known to induce residual stresses depending on the deposition parameters [10]. This implies that significant challenges are related to the fabrication of large area free-standing thin-film electrolytes. One possible solution is to use a sacrificial support material, such as silicon substrates. Other support materials have been suggested, but using silicon makes it possible to take advantage of the well established silicon (semiconductor) fabrication techniques [11]. Microfabrication, or Micro Electro Mechanical Systems (MEMS) fabrication implies bulk and surface micromaching using lithography, wet- and dry etching, and thin film deposition [14]. Micromachining of silicon is possible due to the anisotropic properties of monocrystalline silicon, where the (100) plane is etched up too 400 times faster then (111) planes [14]. This allows for removal of silicon substrate after thin-film deposition, yielding a free-standing membrane. The silicon substrate is preferentially a (100) oriented monocrystal (for subsequent micro-machining purposes), with an insulating oxide layer and a amorphous nitride buffer layer to compensate the thermal expansion mismatch of YSZ and Si ($\alpha_{YSZ} = 10.5E^{-6}K^{-1}$, $\alpha_{Si} = 2.5E^{-6}K^{-1}$ $\alpha_{Si_3Ni_4} = 3.2E^{-6}K^{-1}$[15]). In Fig.4 a relevant example is given.

1.3 Yttria-Stabilized Zirconia (YSZ)

Zirconia is an outstanding material and has been extensively examined for decades due to its remarkable and diverse properties [16]. Zirconia has four major polymorphic modifications, all based on the cubic fluorite structure [16]. At ambient conditions zirconia has a monoclinic crystal structure, while phase transformations take place at around 1170°C and 2370°C (at ambient pressure) to form a tetragonal and cubic phase, respectively [17]. The fourth polymorph is a orthorhombic phase that exist at higher pressures [17]. The monoclinic phase has poor mechanical properties due to the destructive nature of the phase transformation from tetragonal to monoclinic crystal structure, which is associated with an anisotropic volume expansion of 3-5$\%$. This large volume change causes extensive micro-cracking, and pure ZrO_2 is therefor rarely used as an engineering material. The tetragonal and cubic phases exhibit much better mechanical properties, and can be stabilized down to ambient temperature by the addition of a dopant such as yttria [16]. YSZ is hence an oxide composed of zirconia (ZrO_2) and yttria (Y_2O_3).

When zirconia is doped with yttria (or other trivalent cations), the Y^{3+} cations go into solid solution and substitute Zr^{4+} cations in the crystal lattice, resulting in a local loss of one positive charge. To achieve charge balance in the structure, oxygen (anion) vacancies are generated, and the number of vacancies is linearly dependent on the number of dopant atoms and its valence. The presence of oxygen vacancies in the structure lowers the average coordination number of Zr and provides a mechanism to maintain the framework of cubic and tetragonal phases down to room temperature [16]. When doping zirconia with yttria, one can achieve either fully

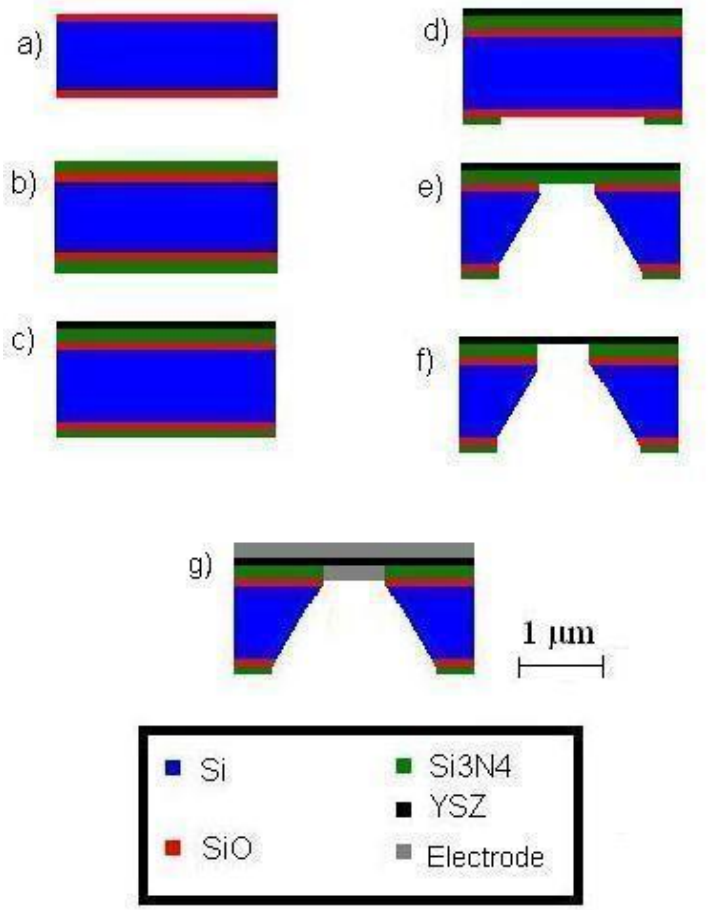

Figure 4: *In a): Si substrate (blue) with a thin SiO oxide layer on both sides (red). b):Deposited silicon nitride on both sides (green). c): Deposited YSZ on one side (black). d): Photolithography and silicon nitride dry etching. e): Silicon oxide and silicon wet etching with HF and KOH, respectively. f): Silicon nitride etching by reactive ion etching, resulting in a YSZ free-standing membrane. g): Sputtering of platinum electrodes (grey) on both sides of the electrolyte, yielding a micro-SOFC membrane [10].*

stabilized zirconia (FSZ), consisting of a pure cubic phase, partially stabilized zirconia (PSZ), consisting of a mixture of tetragonal and cubic phases, or a tetragonal zirconia polycrystal (TZP), consisting almost entirely of the tetragonal phase [16]. The amount of yttria, and the sintering-and cooling temperature decides what phase is stabilized. In Fig. 5a, one can observe the zirconia-rich part of the $ZrO_2 - Y_2O_3$ phase diagram, with the ranges of composition where one can obtain monoclinic, cubic, tetragonal (solid red lines) or mixed tetragonal-monoclinic and tetragonal-cubic (overlopping, dottet red lines), indicated just above the x-axis. When generating oxygen vacancies, one also facilitates ion conductivity. This is why zirconia is an electrically conducting material, as it is capable of carrying O^{2-} through it's lattice by diffusion over a large range of oxygen partial pressures. The conductivity of YSZ depends on the number of charge carriers, increasing by adding more dopant. However, a maximum in ion conductivity of YSZ is found to be at 8-12mol$\%$ Y_2O_3, where further adding of yttria leads to decreasing ion conductivity, see Fig. 5b [18]. For this reason, the state-of-the art electrolyte material for SOFC is zirconia doped with 8 mol $\%$ yttria (8YSZ) [19].

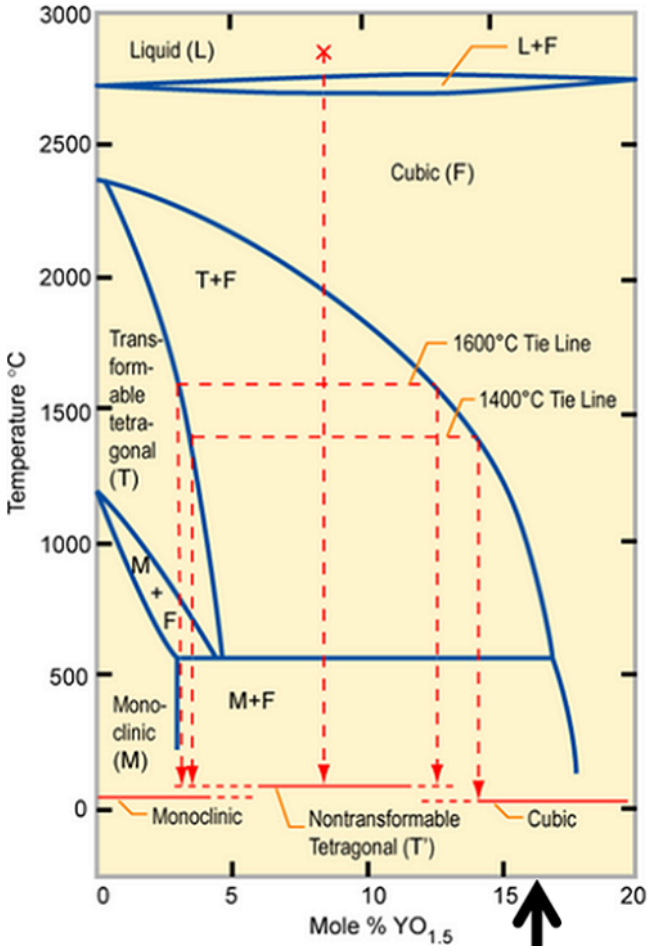

(a) *Zirconia-rich part of the $ZrO_2 - YO_{1.5}$ phase diagram. The black arrow indicates 8YSZ [20]*

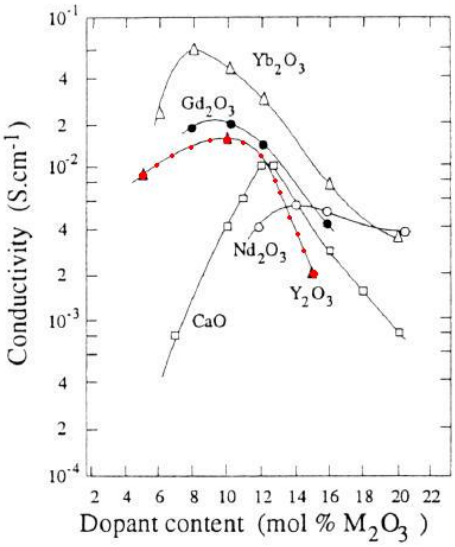

(b) *Dependence of conductivity on composition for ZrO_2-based solid solutions at 800°C. Y_2O_3 is indicated in red [17].*

Figure 5: *Zirconia rich part of the $ZrO_2 - YO_{1.5}$ phase diagram and denpendency of conductivity on YSZ composition.*

1.3.1 Optimal properties of YSZ for micro-SOFC electrolyte applications

Several studies have been made to establish the optimal properties for YSZ thought for micro-SOFC electrolyte applications. Microstructure, stress-state and different target-compositions have been examined and related to the deposition technique to obtain the best mechanical and electrical properties. Achieving a dense and pinhole-free thin-film is the first step towards success [4]. A dense layer is essential to assure that the electrolyte is completely gas tight, while surface defects such as pinholes and locally reduced film thickness must be avoided to prevent short-circuit of the two electrodes or locally higher current densities resulting in hot-spots [1].

Electrical conductivity of YSZ is higher in the bulk then in the grain boundaries [1]. Thus, columnar grains spanning the whole electrolyte thickness is preferential, to virtually eliminate the grain boundary contribution. This is achieved when PLD deposition is performed at substrate temperatures higher then 400°C, see Fig. 6 [21]. Crystallinity and grain connectivity (density) increases further with temperature [10]. This phenomenon will be given more atten-

tion in the section about PLD.

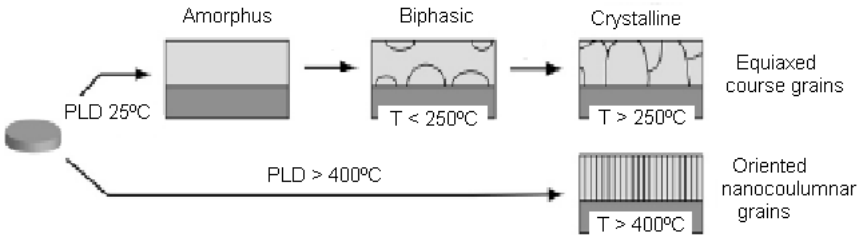

Figure 6: *YSZ grain growth as a function of substrate temperature in Pulsed Laser Deposition [21].*

Apart from a dense, columnar and homogeneous film, the YSZ electrolyte should have the highest possible mechanical strength. However, stress is induced in the YSZ thin-film when deposited by high energy processes such as PLD. Compressive stresses are induced during deposition due to particles arriving with a high kinetic energy (atomic peening). This phenomenon is more critical at low deposition temperatures (below 400°C), because at higher temperatures a recovery processes by vacancy, interstitial and dislocation movement actively improves the mechanical properties of the thin-film [10].

The stress-state of thin-film YSZ affects the conductivity, as stress induces strain in the lattice. Lattice strain can affect the local change in space along the ionic migration path and the interatomic bond strength between the migrating oxygen ions and the nearest neighbor cation [22]. It is found that higher strains of the material yields higher conductivities, meaning that a more distorted lattice facilitates ionic diffusion [22]. Thus, the stress-state of the as-deposted YSZ electrolytes can be considered as fortunate with respect to conductivity.

The deposition temperature used in this project (600°C) is a compromise between achieving high crystallinity, an acceptable stress-state and keeping the deposition temperature within the operating temperature of the thought micro-SOFC system.

1.4 Pulsed Laser Deposition

1.4.1 Introduction to the PLD technique

Pulsed Laser Deposition (PLD) is versatile material thin-film processing technique based on laser ablation of a target material onto a substrate. The PLD system comprises a laser, a set of optical components used to focus the laser beam onto the target surface, and an Ultra High Vacuum (UHV) chamber where the target and substrate are located opposite to each other. One of the major benefits of the PLD technique is the decoupling of the UHV chamber and the evaporation power source (the laser), enabling to choose the ambient background gas and pressure during deposition [23]. A relevant example is the introduction of oxygen into the UHV chamber during deposition of YSZ, to assure sufficient oxygen in the structure [5].

The basic idea of the technique is to evaporate a small amount of material from the target surface with a pulsed, focused laser beam. The evaporated material is ejected normal to the target surface towards the substrate (due to the rapid built-up of a pressure gradient) and deposits by condensation on the substrate surface [3]. The film-growth normally takes place far from thermodynamic equilibrium, as the substrate temperature is typically much lower then the

melting temperate of the target material. This enables growth of metastable phases and artificial structures [24].

The PLD process also allows for stoichiometric transfer of the target material onto the substrate. This is because the pulsed laser beam heats the target so quickly ($10^{12}\ K/s$) that all target material components evaporate at the same time, irrespectively of the partial binding energies [5]. This, combined with the possibility to choose the background gas in the UHV chamber, makes it possible to deposit all kinds of materials, like high temperature superconductors, metals, oxides, nitrides, carbides, polymers etc [5]. Conventional PLD has been effectively limited to small substrates, while large area PLD now allows for deposition on larger substrates (up to 8 inches in diameter [6]) by using dynamic mirrors and lenses.

1.4.2 PLD material ablation and film growth

As the laser pulse induces extremely rapid heating of a small volume in the target surface, material ejection begins on a picosecond time-scale [25]. The ablation is governed by two distinct processes; electronic and thermal sputtering [26]. The electronic sputtering is a chain of processes initiated by the incident photons producing electron-hole pairs and electronic excitation, which energy is quickly transferred to the crystal lattice. This leads to a strong heating of the lattice, and massive particle emission from the target surface [3]. Thermal sputtering is an equilibrium process where the laser energy is adsorbed and melts a small volume of the target material, producing a high pressurized gas as further heating evaporates the melted material. A supersonic jet of particles is ejected normal to the target surface as a result of the pressure gradient. The thermal sputtering requires more time (nanoseconds), but will dominate when using longer pulse durations [25], which is the case in this project. In Fig.7 one can see the typical shape of the plume of ejected particles in both thermal and electronic sputtering.

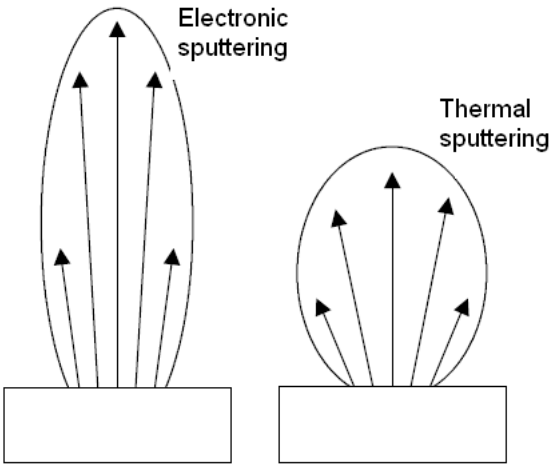

Figure 7: *Figurative image of the plume in electronic and thermal sputtering [23].*

Unless one is working with very short pulse durations, the plume will be continuously irradiated after ejection. This radiation will be adsorbed by the ejected particles, leading to excitations and ionization of the irradiated species and the formation of a plasma [25]. Subsequent recombination processes in the plasma causes fluorescence and is visible to the human eye [3]. The

expansion of the plume is a beam-like, forward jet of uniform translational energy with small spread similar to those of a high pressure gas via a narrow nozzle [23]. When the particles reach the substrate and condense, film growth characteristics are much dependent on substrate temperature and the mobility of the incident particles.

The film growth is frequently three dimensional islands-growth, also called Volmer-Weber growth [24]. Initial nucleation of small clusters of atoms evolve into stable nucleus which grow in the z-direction upon further bombardment of particles. The initial in-plane grain size is determined by the saturation nucleation density and nucleation kinetics [24]. The film growth generally takes place far from thermodynamic equilibrium, and the microstructure changes with film-thickness as competitive growth between planes of different densities and free energy develops [27] [24]. Growth of preferred orientation and extinction of others due to shadowing is well known for columnar growth of crystalline materials, and may yield hollow channels in the microstructure [27].

Cubic YSZ grown on amorphous substrates has a preferential (111)-orientation (meaning that the (111) plane is parallel with the substrate), as this plane has the lowest interface energy with the substrate [18]. The (111) plane is also the plane of highest density, which is observed to be another property associated with preferred orientation in columnar growth [18]. However, the (200) plane grows faster then the (111) plane [27], which favors this orientation with increasing film-thickness if the mobility of the incoming particles is too low for significant surface diffusion to the the lower energy (111)-oriented grains [24]. As the grains grow longer, nucleation of new grains on top of columnar grains may occur, as growth instability is known to increase with increasing length of the grains. The orientation of the new-formed grains will be less influenced by the substrate, as the importance of surface energy decreases with increasing film thickness [28]. One can identify a preferred orientation by comparing the XRD results of a deposited film to the XRD reference pattern of bulk material. The reference pattern for 8YSZ is presented in Fig.8.

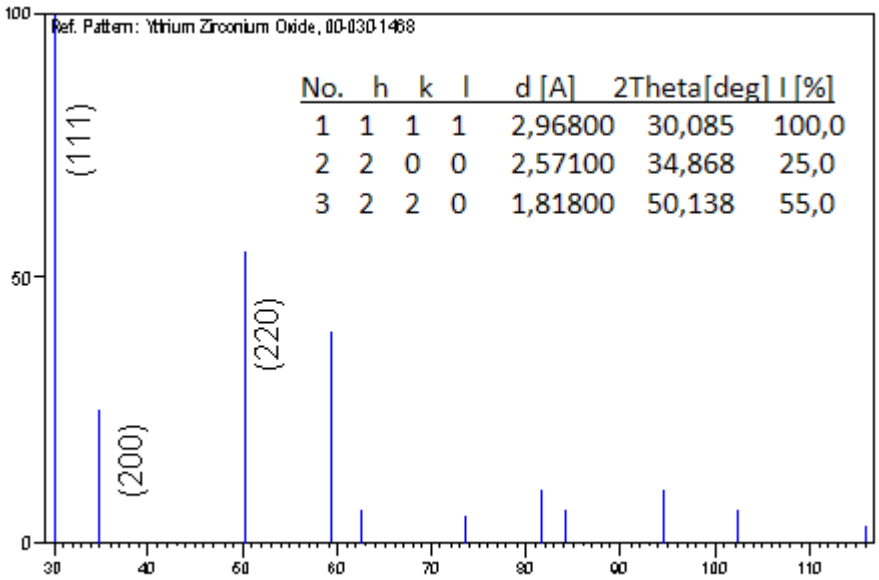

Figure 8: *XRD reference pattern and relavtive intensity of the three first peaks in bulk 8YSZ [29].*

1.4.3 Paramteres and versatility of the PLD process

The PLD process is a versatile technique because many experimental parameters can be changed to influence the properties of the deposited material [5]. Important parameters such as substrate temperature, gas pressure (P_{O_2} in the case of deposition of YSZ), WD and laser fluence affect the as-deposited film-properties such as thickness, density, homogenity and microstructure.

Two of the most important parameters are the substrate temperature and the background pressure during deposition. Substrate temperature is decisive for thin-film microstructure due to the dependency of surface and bulk diffusion on temperature. Structure zone models (SZM) have been developed to systematically categorize the influence of deposition temperature on microstructure for physical vapor deposition techniques such as PLD [24]. The models are based on the relationship between the $reduced\ temperature$, T_R, which is defined as the deposition (substrate) temperature, T_S, divided by the melting temperature of the target material, T_M [4]. The three zones were defined by Thornton (1974) as the following [4] [30]:

Zone 1: $T_R < 0.3$: The thermal energy of incoming species is too low for significant surface diffusion, columns preserve the random orientation of the nuclei. Atomic shadowing and limited surface diffusion leads to extensive porosity.

Zone 2: $0.3 < T_R < 0.5$: Significant surface diffusion leads to a polycrystalline, dense columnar structure.

Zone 3: $T_R > 0.5$. Bulk diffusion and enhancement of crystallization and grain growth.

These three zones are based on the influence of temperature alone, but bacground pressure can affect the boundaries in the model here presented, i.e. a transition zone can be created between zone 1 and 2 by lowering the deposition pressure. This is very helpful in the deposition of YSZ thin-films, as the melting temperature of YSZ is above 2500°C [4].

The pressure of the ambient gas during deposition has such a significant role because it influences the plume dynamics. The ejected particles in the plume will collide with the gas molecules upon which they scatter and thermalize. The spatial distribution, deposition rate and the kinetic energy of the different species will therefore decrease with increasing pressure [5].

It has been reported by A. Infortuna et al. that dense films of YSZ can be produced at high temperatures (1500 °C) in ambient pressure, but by lowering the P_{O_2} to below 37 mTorr, dense films can be achieved at a deposition temperature of 400°C [4]. In Fig. 9 one can observe the combined effect of temperature and pressure in the temperature range $T_R < 0.5$.

The laser fluence (the energy density of the laser beam at the target material,$[mJ/cm^2]$) mainly affects the deposition rate. The size of the plume increases with increasing laser fluence as more target material is evaporated and ablated. The laser flunce also influences the kinetic and thermal energy of the ablated species, but the importance of laser fluence on this is small compared to the importance of ambient pressure [5].

The WD (target-substrate distance) represents another important parameter. There are two considerations: the first is to adjust the energy of the incoming particles to an appropriate value. A good starting point is to assure that the plume tip touches the substrate [5]. The second is to keep the element ratios in the film as close as possible to those in the target. This is however not a problem when depositing YSZ, as Y and Z have very similar mass [27]. Other deposition parameters that influence the ablation rate and the as-deposited film are the laser photon energy (must be higher then the target material bandgap E_g), laser pulse frequency $[Hz]$, total number of pulses and the wavelength of the laser [3].

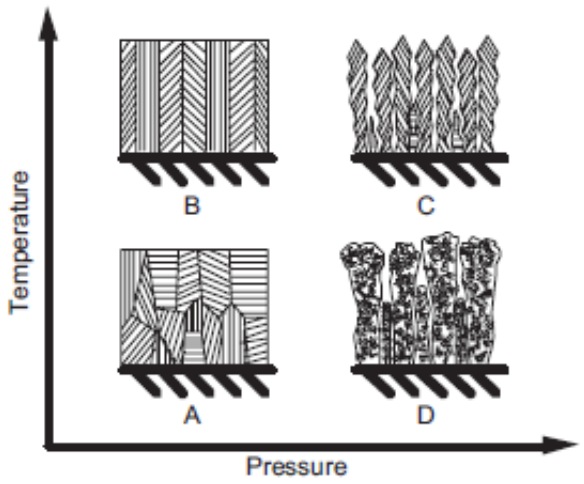

Figure 9: *The effect of temperature and pressure of YSZ thin-film microstructure. In A, a low pressure and a moderate temperature yields a dense, polycrystalline structure due to significant surface diffusion. In B, higher temperatures yields even more significant surface diffusion, and strongly ordered grains form a dense structure. In C, at high pressure and temperature, columnar grains spanning the whole film thickness are formed due to moderate surface diffusion, but shadowing effects prevent full density. In D, at low temperatures and high pressures, accumulation of loosely packed clusters of atoms form in a columnar, porous structure [5]. In this figure, A corresponds to a transition zone between zone 1 and 2, B corresponds to zone 2 and D and C correspond to zone 1.*

1.4.4 Problems related to target-laser interactions

As target material is ablated during deposition, two morphological changes take place on the target surface; gross deformation and cone formation [3]. In the first case, repeated material ablation of a rotating target leaves a trench in the target surface, which with time will change the projection area of the laser spot and hence, the fluence. This will lead to a tilted plume, which will offset the plume which originally would be centered on the substrate. In the second case, the structure of the target surface will change on a microscale, as repeated melting and cooling of the target surface leads to recrystallization and cone formation, see Fig.10 d). The formation of cones might also tilt the plume, but this effect is much slower than the tilting caused by trench formation. To avoid both these effects, it is fortunate to use larger targets, and to both rotate and move the target the x-direction (apply target rastering), see Fig11. In this project, target rotation and rastering was applied in each deposit.

Ejection of larger particles from the target is a significant problem for the PLD technique [1]. There are four major causes for the formation of larger particulates and smaller droplets: exfoliation (i), stress-induced material breakdown, yielding fragments of irregular shapes and sizes (ii), explosive boiling, yielding spherical droplets in the micrometer range (iii) [25] and collision of elements in the plume, forming small, spherical nanoclusters with dimensions from 10 to 50 nm (iiii) [4]. Exfoliation occurs when high pressurized gas expands and breaks loose solid fragments of the target. Stress-induced material breakdown is a consequence of the repeated heating and cooling of the material, inducing stresses due to the expansion and contraction of the material. This makes the target fragile, and further laser pulses lead to exfoliation. Explo-

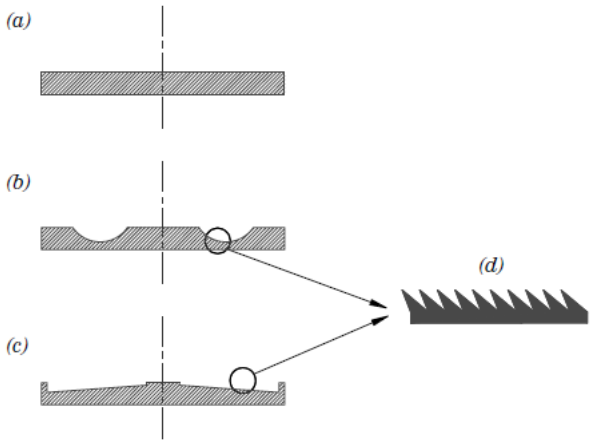

Figure 10: *Figurative explanation of how the target surface changes during deposition. a) A new target. b) Target after deposition, where the laser spot has been fixed, while the target has been rotating. c) Target after deposition when the plume has been fixed, while the target has been rotated and moved in the x-direction (target rastering). d) Microscopic morphology changes due to the laser beam. The cones will point back in the direction of the incident laser beam [6].*

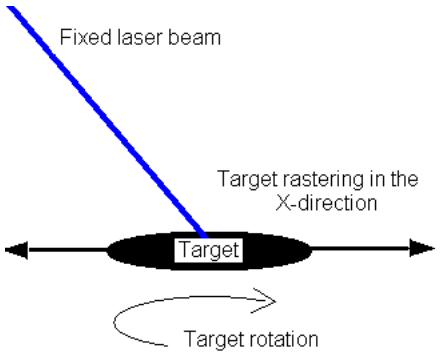

Figure 11: *Target rastering. Rotation and movement in X-direction under a fixed laser beam helps to minimize the trenching and cone-formation effect on the target surface.*

sive boiling is the ejection of molten material when the laser fluence is above a threshold value, where material in the liquid state is ejected towards the substrate.

Nanoclusters is a phenomenon residing from the influence of ambient gas pressure (oxygen pressure in deposition of YSZ) on the plume dynamics. The presence of a gas limits the plume expansion and increases the probability of collision between the ablated species, as the plume becomes more and more saturated with particles at higher pressures. The saturation facilitates the nucleation and growth of nano-sized clusters in the plume. These clusters reach the substrate surface with a given energy (thermal + kinetic energy) and if this value is below a threshold value, they maintain their shape and size, while above the threshold value, they dissociate [4]. Common for all these particulates, is that they induce surface defects. They may also exert a shadowing effect, reducing the film thickness in there immediate surroundings, see Fig. 12.

To avoid exfoliation and stress-induced material breakdown, using a target material with small grain size and optimized mechanical properties is beneficial. In the case of YSZ, spark plasma sintered YSZ with 3 mol $\%$ yttria (tetragonal phase with smaller grain size) have been

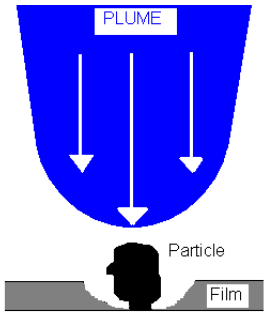

Figure 12: *Shadowing effect of particles on the substrate surface*

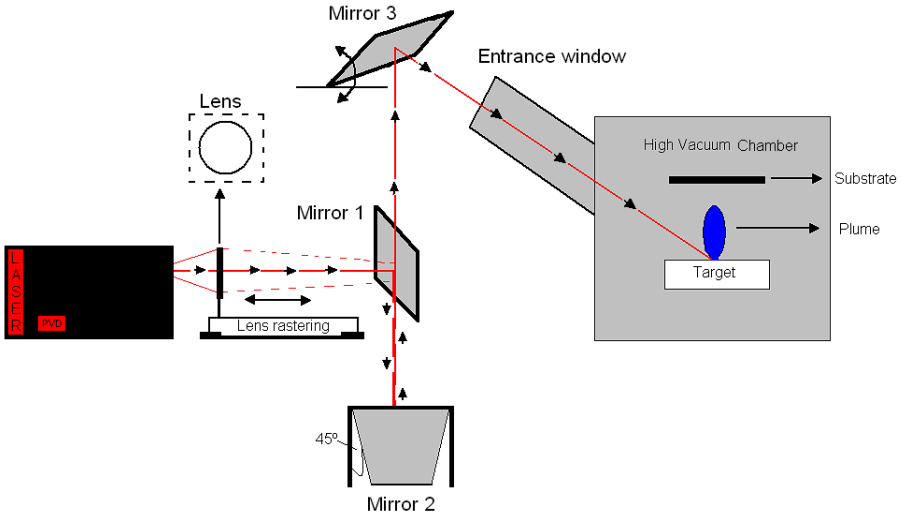

Figure 13: *Path of the laser beam in a large area PLD-device*

proven to reduce such particles [1]. To avoid nanoclusters and explosive boiling, one must tune the gas pressure and laser fluence during deposition, respectively.

1.4.5 Large area PLD

Large area PLD is needed for an up-scaling of the PLD process. The major difference between a conventional PLD and a large area PLD is that the large area PLD comes with a programmable raster mirror, allowing to sweap the laser beam over the target surface. The optical system of a large area PLD consist of a focal lens and high reflecting mirrors, where the last mirror in the laser path is dynamic. The path of the laser beam for the PLD-device used in this project can be observed in Fig. 13.

The focal lens from Fig.13 is mounted on a device that allows for movement in the x-direction. The focal lens and the dynamic mirror (mirror 3 in Fig.13) are linearly correlated, so that the distance from the focal lens to the target surface is constant, maintaining a fixed laser spot size, and thus, a fixed laser fluence during deposition. The principle of how this mirror rastering works is explained figuratively in Fig. 14

Some of the problems related to up-scaling of the PLD technique have to do with achieving a homogeneous film thickness. Power and beam stability, proper design of the optical components, robust substrate heaters, large target size and motion are issues that must be optimized to

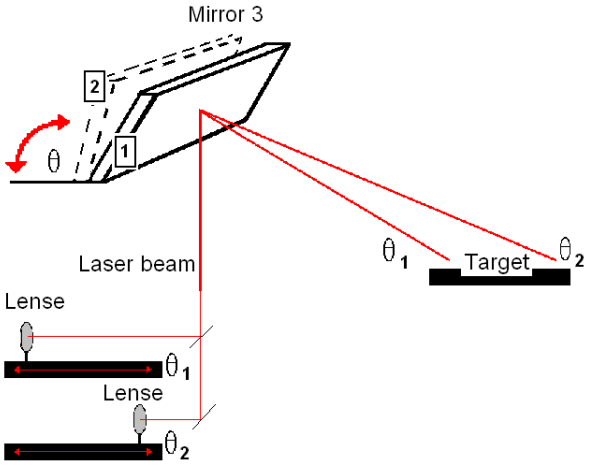

Figure 14: *Mirror rastering by changing the angle (θ) of mirror 3. Position 1 and 2 of the mirror and lense corresponds to the incident beams θ_1 and θ_2 on the target, respectively. The lens moves in correlation with the mirror to maintain the distance from the lense to the target surface, maintaining the laser spot size*

avoid variations of important parameters such as laser fluence and substrate temperature [5].

1.4.6 Excimer lasers

The PLD-device used in this project makes use of an Excimer laser as the energy source. The term Excimer is the short of "excited dimer", which means a compound of two species that exist only in the excited state [31]. The excimer laser gain medium (a medium which can amplify the power of light) is a mixture of gases, typically containing a noble gas (e.g. argon, krypton or xenon) and a halogen (e.g. fluorine or chlorine). The gain medium is pumped with short current-pulses in a high-voltage electric discharge, which creates excited dimers. This occurs because, for a brief moment (nanoseconds), the noble gas is ionized and attract the neutral atoms such as fluorine or chlorine, and form ionized molecules (excimer complexes) [32]. Typical excimer complexes are krypton fluoride (KrF), xenon fluoride (XeF), argon fluoride (ArF) and xenon chloride (XeCl). The bond between the atoms in an excimer complex is very strong, but can only last for a few nanoseconds, until the noble gas atoms are no longer excited. The molecules will then dissociate, and the binding energy is released in the form of photon energy [31]. The photons released form a laser beam of a specific wavelength, and the stronger the binding energy, the shorter the wavelength, e.g. AsF has a wavelength of 193 nm while KrF has a wavelength of 248 nm [32]. The photon energy of a KrF excimer laser is 5.0 eV [33].

2 Experimental methods

2.1 Pulsed Laser Deposition of YSZ on silicon-based chips

YSZ thin films were deposited by the PLD device at IREC, a PLD 5000 (PVD Products) with a Lambda Physic COMPex PRO 205 Excimer laser with KrF gas, yielding a wavelength of 248 nm and a pulse duration of 20 ns [34]. A black body, oxygen resistant substrate heater placed inside the UHV chamber was used to keep the substrate at desired temperature, using infrared heat lamps and a water cooling system. The PLD 5000 can be observed in Fig. 15a.

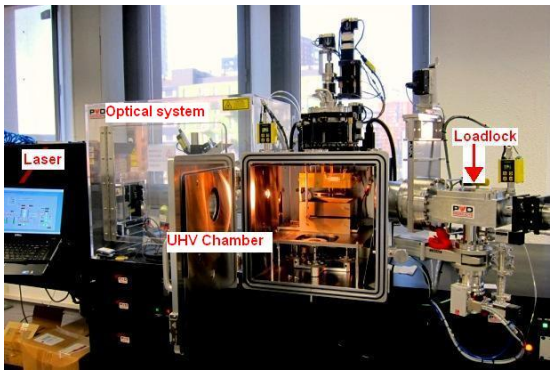

(a) *The PLD 5000 with the laser, UHV-chamber, optical system and loadlock indicated*

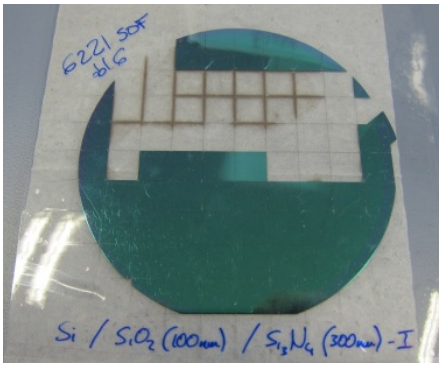

(b) *The Si-based chips, cut from a 4 inch $Si/SiO_2/Si_3N_4$ wafer*

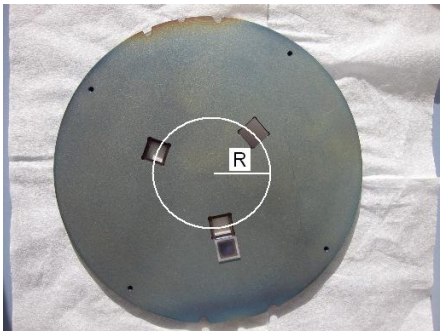

(c) *PLD substrate holder for chips. The white circle represents the movement of the chip during deposition (Moves in a circle with a radius (R) of 1 inch).*

Figure 15: *Photos of the PLD 5000, Si-based chips and chip-substrateholder*

The substrate material used was monocrystalline silicon chips with a (100) orientation prepared at The National Center of Microelectronics (CNM) in Catalunya. The chips measured 1x1 cm and had a thickness of 300 μm. The chips were multilayered, with a 100 nm thick silicon oxide layer (obtained by oxidation) and a 300 nm thick silicon nitride layer (obtained by low pressure CVD) on both sides, yielding a $Si/SiO_2/Si_3N_4$ layered structure. The chips had been cut from a larger wafer, as can be seen in Fig. 15b, to fit in the PLD substrate-holder, see Fig. 15c. The chips were washed, cleaned (in acetone, isopropanol and distilled water) and dried with pressurized gas (nitrogen) before deposition. The substrates were introduced into the UHV chamber thorough the load-lock, and heated to 600$^\circ C$ with a ramp rate of 30$^\circ C$/s.

The pressure inside the UHV chamber had a maximum value of 10^{-6} mTorr before oxygen was introduced. During deposition, the substrate holder was rotated with a velocity of 5 rpm, indicating that the substrate moved in a circle with a radius corresponding to the distance from the center of the substrate holder to the chip-position (1 inch, or 2, 54 cm), see Fig. 15c. The plume position was fixed and always coincided with the rotating substrate in a point lying on the circle indicated in Fig. 15c.

The target material was a sintered pellet of FSZ (fully stabilized ziconia) doped with 8 mol$\%$ yttria (8YSZ) produced at IREC (powder delivered by MEL Chemicals). The pellet had a diameter of 3 inch (7,62 cm). During deposition the target was rotated with a velocity of 15 rpm, and a computed rastering program provided movement of the target in the x-direction. In the first series of deposition, the laser energy was held fixed, while P_{O_2} and WD (target-substrate distance) were systematically changed between 50, 100 and 150 mTorr and 90, 110 and 130 mm respectively. The choice of these initial parameters were chosen with respect to the characteristics of the PLD 5000, where the minimum possible WD was 90 mm and a minimum pressure of 50 mTorr was recommended by PVD Products. In a later stage, deposition of YSZ was performed with pressures down to 20 mTorr. An overview of deposition parameters (P_{O_2}, WD, laser fluence and total amount of laser pulses) for all samples is given in Table 1.

Sample	P_{O_2} $[mTorr]$	WD $[mm]$	$Fluence$ $[mJ/cm^2]$	$Pulses$
$Y05$	100	110	976	40000
$Y06$	50	110	976	40000
$Y07$	150	110	976	40000
$Y08$	90	110	976	40000
$Y12$	150	90	976	40000
$Y13$	50	130	726	40000
$Y14$	100	130	722	40000
$Y15$	150	130	716	40000
$Y22$	25	110	725	40000
$Y23$	25	130	725	40000
$Y25$	35	90	725	40000
$Y26$	50	90	725	40000
$Y28$	30	90	700	40000
$Y29$	25	90	725	40000
$Y30$	20	90	725	40000
$Y31$	20	110	725	40000
$Y32$	20	130	725	40000
$Y33$	100	90	725	80 000

Table 1: *Deposition parameters*

2.2 Film thickness measurement by reflectometry

All samples were brought to CNM for thin-film thickness measurements in a Nanospec 6100 refelctometry device (Nanometrics). The device used light with increasing wavelengths from 400-800 nm to scan the transparent YSZ-thin film, while measures the resulting reflectance

versus wavelength and, from this data, determined the film-thickness. The thickness of each sample was measured in the middle of the chip, as some shadowing effects were expected from the sample holder on the chip extremes. Due to similar optical properties of YSZ and silicon nitride, the refelctometry device did not always differentiate between these two layers. This was however corrected, as the thickness of the nitride-layer was known to be 300 nm.

2.3 XRD analysis

All samples were analyzed in a Bruker D8 Advanced using standard copper α-radiation and a nickel filter. All the samples were analyzed using the same parameters. Scanning was performed with 2 theta values ranging from 20-55° with an increment of 0,02. An offset was applied to avoid obtaining a diffraction pattern from the monocrystalline silicon substrate. This was done by choosing the offset coupled theta configuration, allowing one to set both the theta and two-theta start values, which were set to 9 and 20, respectively.

2.4 Scanning Electron Microscopy (SEM) analysis

2.4.1 Planar view

All sample-surfaces were imaged in a Zeiss Auriga SEM-device. The samples were mounted on metallic SEM sample holders with conductive tape before being introduced into the SEM. Planar images at various magnifications up to x 100 000 were taken of each sample, applying 40 μA current and a voltage of 1 kV to avoid charging of the non electron-conductive YSZ layer. For the planar imaging, the mode of secondary electrons was chosen.

2.4.2 Cross sectional view

Samples were coated with silver paste and cut in half with a diamond cutter before being mounted on conductive tape on metallic SEM sample holders to examine cross sections. The images were taken with InLense field emission microscopy in the same SEM-device as previously mentioned. Short working distances (approximately 1 mm) and low voltages (1-2 kV) were applied to minimize the charging of the samples, even though they were coated with conductive silver paste.

2.5 TEM sample preparation and analysis

One sample (sample Y29, deposited at 90 mm WD and 25 mTorr) was prepared for TEM cross-section analysis at Universitat Autonoma de Barcelona (UAB), where the required instruments for TEM sample preparation was procured.

The first step in the sample preparation was to cut a 3 mm wide strip from the middle of the as-deposited chip with a saw (Struers), using a diamond coated blade. To enable the cutting, the chip was mounted on a piece of glass using melted wax as glue, see Fig. 16a.

The 3 mm wide strip was cut into 2 pieces of 1x3 mm using the same technique. After cutting, the samples were left in acetone for 5-10 min to remove the wax. The next step was to glue two of the 3x1 mm samples together with epoxy, with the YSZ layers facing each other, and leaving the epoxy to polymerize (at least 2 hours). The resulting sample was a "sandwich"

which was polished down to 60 μm using 800 SiC polishing paper and a Gatan disc grinder (see Fig. 16b) to control the thickness of the sample.

In the next step, a Gatan dimple grinder was used to make a dimple in the the middle of the sample, with a minimum thickness of 25 μm. Diamond paste and water soluble coolant (lubrication) was applied for the grinding process. When accomplished, the sample was detached from the sample holder in acetone and glued on TEM copper substrate holders with epoxy. The sample was left for 2 hours to allow polymerization.

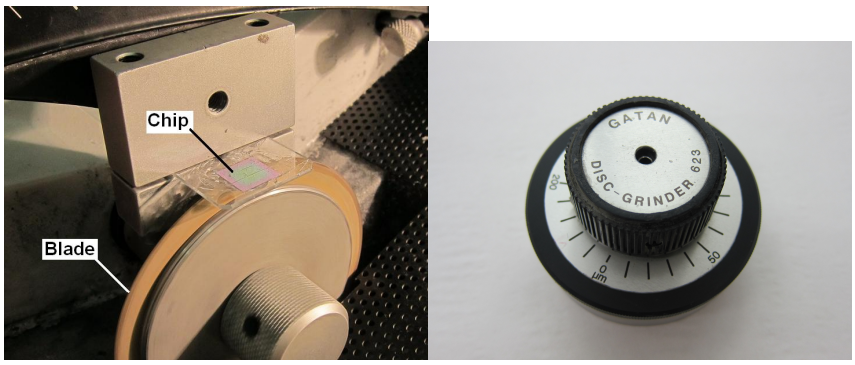

(a) *Cutting of a 3 mm strip from a chip* **(b)** *Gatan Disc grinder*

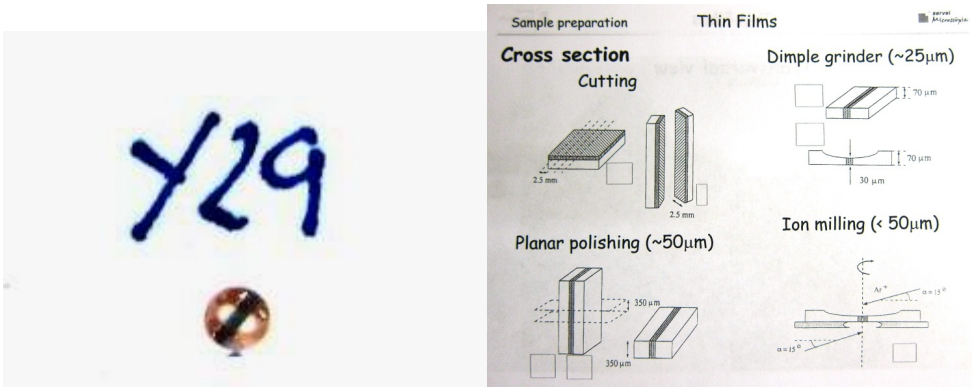

(c) *Prepared sample* **(d)** *Thin-film sample preparation*

Figure 16: *TEM sample preparation*

The last step of the TEM sample preparation was ion milling with a Gatan Precision Ion Polishing System (PIPS). The PIPS milled with two argon ion beams, and the voltage was set to 4 keV. The pressure was $8E^{-5}$ Torr, the sample rotation was set to 3 rpm and both gun angles were set to 6 °. The sample was milled down until a hole was visible in the middle of the dimple, knowing that the sample thickness in the immediate range of the hole was sufficiently thin for electron transparency. The prepared sample can be seen in Fig. 16c. An overview of the sample preparation method can be observed i Fig. 16d. The TEM analysis was performed in a Jeol 220 microscope applying an operating voltage of 200 kV.

2.6 Pulsed Laser Deposition of YSZ on 4 inch (10 cm) wafers

Four silicon-based wafers were deposited with YSZ using mirror rastering, allowing movement of the laser plume in the x-direction. Different rastering velocities and intervals were applied,

to find the optimal rastering conditions to achieve a homogeneous film-thickness. The wafers were monocrystalline silicon with a (100) orientation, except from wafer 3 which had the same Si/SiO/Si_3N_4 structure as the silicon-based chips previously used. During deposition both the wafer and the target were rotated (note, the target was only rotated, and not moved in the x-direction as previously) with a velocity of 5 and 15 rpm, respectively. In Table 2 one can see the deposition parameters used for each wafer. In Table 3, one can see the relative velocity in different intervals on the target. V1, V2 etc correspond to the velocity, $[mm/s]$, of the movement of the mirror rastering in a given interval. R1, R2, R3 etc correspond to the distance from the center of the $wafer$. The target was 3 inches (7.62 cm) in diameter, while the wafers were 4 inches (10 cm) in diameter. The mirror rastering was applied on half of the target in wafer 1, 2 and 3. While mirror rastering corresponding to the half of the wafer was applied in wafer 4, see Fig. 17.

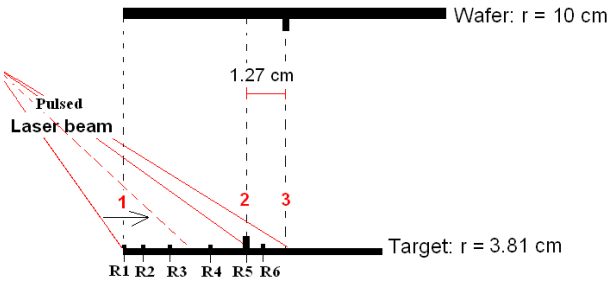

Figure 17: *Mirror rastering of half the target (from point 1 to 2) or half the wafer (from point 1 to 3). The wafer and target were aligned so that their edges were placed directly over each other, and the center of the target was displaced 1.27 cm to the left of the center of the wafer. The laser beam moved with increasing velocity from the edge of the target towards the center. The distance between R1, R2 etc represent the intervals of a given velocity.*

Wafer	P_{O_2} $[mTorr]$	WD $[mm]$	$Fluence$ $[mJ/cm^2]$	$Pulses$
$Wafer\ 1$	150	90	-	80000
$Wafer\ 2$	100	110	800	80000
$Wafer\ 3$	20	90	725	80000
$Wafer\ 4$	25	90	725	80000

Table 2: *Deposition parameters for wafer 1-4*

$Wafer$	R_2	R_3	R_4	R_5	R_6	V_{R1-R2}	V_{R2-R3}	V_{R3-R4}	V_{R4-R5}	V_{R5-R6}
W_1	4.65	3.9	3	1.5	1.27	0.1	0.11	0.14	3	-
W_2	4.49	3.89	3.09	1.27	-	0.08	0.11	0.19	1.11	-
W_3	4.57	4.06	2.866	1.669	1.27	0.004	0.011	0.02	0.12	3
W_4	4.75	2	0.6	0	-	0.008	0.22	0.3	3	-

Table 3: *Intervals (R), $[cm]$ and relative velocity (V) of mirror rastering. R1 was 5 cm in all deposits.*

3 Results and discussion

All chips were successfully deposited with 8YSZ. The presence of a thin-film was identified on each sample with the human eye, as seen in Fig. 18. The optical properties of YSZ changes with film thickness, which is why the chips in Fig. 18 have different aspects.

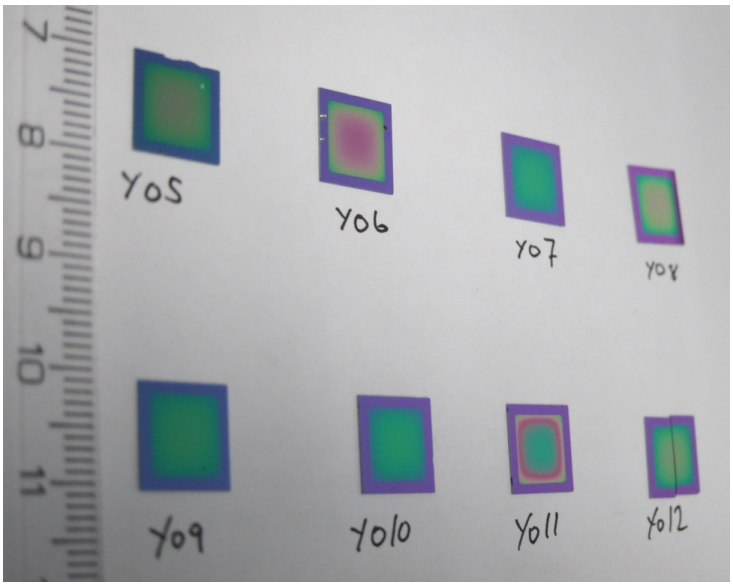

Figure 18: *Photograph of samples Y05-Y12 deposited with YSZ*

3.1 Thin-film thickness on chips

On overview of the YSZ thin-film thickness measured on all samples can be observed in Fig. 19a and 19b. The thickest layer of YSZ measured 239 nm (sample Y30) while the thinnest layer had a thickness of 15 nm (sample Y15). These two extremes correspond to the thickness of the two samples deposited with the lowest and highest P_{O_2} at the closets and furthest WD, respectively. As all samples were deposited applying the same amount of laser pulses (implying that similar amounts of target material was ablated during each deposit), the significant variation in thin-film thickness reflects the great influence deposition parameters have on plume dynamics and deposition rate.

The depositions rate in this project is difficult to compare to values available in theory, as the substrate holder was rotating in a circle with a radius of 1 inch (2.54 cm) while the plume was fixed. This configuration implies that much ablated material have deposited onto the substrate holder, i.e. the deposition rates would be very low compared to deposits where the plume is centered just below the substrate. However, as each deposit was performed with the same substrate holder and rotation velocity, a variation in film thickness indicates a variation in deposition rate.

The thickness of the thin-film layer decrease as a function of both increasing WD and increasing P_{O_2}, see Fig. 19c and 19d. The thickness decreases linearly with increasing WD, and exponentially with increasing pressure. In Fig. 19c the dependency on WD is similar for samples deposited at 20 and 25 mTorr, while samples deposited in 50 mTorr (blue line), has a

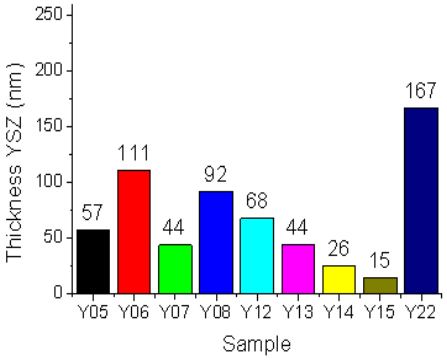

(a) *Thickness of deposited YSZ on samples Y05-Y22*

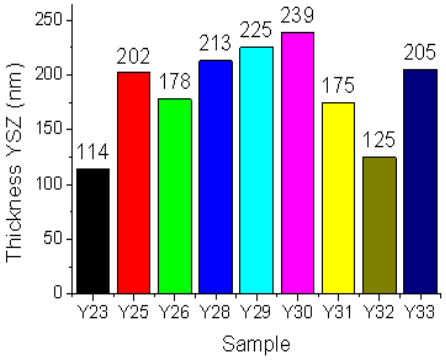

(b) *Thickness of deposited YSZ on samples Y23-Y33*

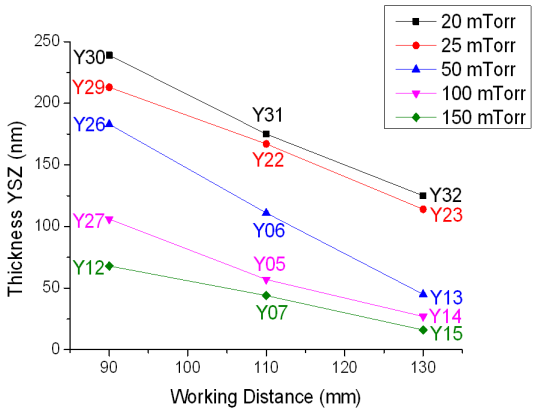

(c) *Thickness of deposited YSZ as a function of WD*

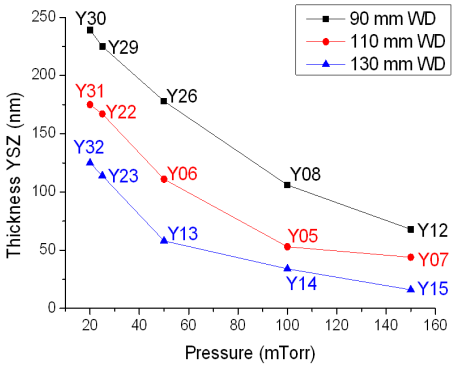

(d) *Thickness of deposited YSZ as a function of* P_{O_2}

Figure 19: *Thin-film thickness of as-deposited samples*

steeper slope. Samples deposited at 100 and 150 mTorr have a similar slope, but they appear less dependent on WD than for samples deposited at lower pressures (their slope is less steep).

In Fig. 19d a steeper slope is also detected around 50 mTorr for all WD's. These observations are important, as they suggest that above 50 mTorr the plume of ablated material is out of reach of the substrate, yielding very low deposition rates.

The observations here commented are in accordance with theory, as higher pressure (more oxygen molecules in the plume-path) yields higher scattering and lower kinetic energy of the particles in the plume, effectively hindering more particles to reach the substrate surface. The influence the WD has on the film-thickness is also reasonable, because at a given P_{O_2}, increasing the WD increases the distance the species in the plume must travel, resulting in more scattering and thus a lower deposition rate.

3.2 XRD-results

The presence of crystalline YSZ was identified on all substrates after deposition, see Fig. 20. From the XRD results presented it is clear that film-thickness influence the intensity of the XRD peaks. This is reasonable, as a thicker film yields more material to diffract upon, leading to a superior number of counts. This implies that it is problematic to compare crystallinity between

layers of a distinct thickness from the XRD results alone.

The relative intensity of the peaks, however, are comparable, and tell something about preferred orientation. It is clear that all of the samples have some degree of preferred orientation, as none of the YSZ thin-films have the same relative peak-intensity in their XRD pattern as the reference XRD pattern for bulk-8YSZ shown in Fig. 8. This is expected, as preferential growth is a known phenomenon in columnar growth.

A general tendency in Fig. 20 is that the intensity of the (111) peak increases relatively to the (200) and (220) peaks with decreasing pressure. This implies that a (111) orientation is favored with decreasing pressure. There are however exceptions, such as sample Y12 and Y08 (WD of 90 mm and a P_{O_2} of 150 and 100 mTorr, respectively), where the (200) peak have the most counts. The (220) peak has a lower intensity compared to the bulk 8YSZ in all the diffraction patterns presented in Fig. 20.

A possible theoretical interpretation of the XRD results presented i Fig. 20 is that at higher pressures (100 and 150 mTorr), the kinetic energy of the ablated material is too low for significant surface diffusion. An initial nucleation, favoring grains with a (111) orientation (see sample Y14 and Y15, Fig. 20), is followed by a gradual dominance of the faster growing (200) oriented grains with increasing film thickness, see sample Y07 and Y12 (150 mTorr) and sample Y05 and Y08 (100 mTorr) in Fig. 20. The phenomenon that the (200) orientation gradually dominates with increasing film thickness when the ablated material that reach the substrate surface have reduced mobility is also reported by Xiong Xuming et al. in reference [27].

At 50 mTorr the same tendency towards a (200) orientation with increased film thickness is observed for the two samples deposited at a WD of 130 and 110 mm. The sample deposited at a WD of 90 mm (sample Y26), however, show a clear (111) orientation. This implies that the WD is decisive for the microstructure at this pressure, supporting the discussion from the previous section that at around 50 mTorr an important change takes place in the plume dynamics (i.e. the plume expands sufficiently to reach the substrate), which also seems to affect the microstructure.

Samples deposited at 20 and 25 mTorr have a (111) oriented structure, with the relative intensity of the (200) and (220) peaks showing a tendency to increase with shorter WD. This might be because film thickness also increases with decreasing WD, and the development of a XRD pattern more similar to bulk-8YSZ (presented in Fig. 8) is a result of growth instability of the columns, and the nucleation of new grains that take on a more random orientation distribution as the substrate interface energy no longer plays a role.

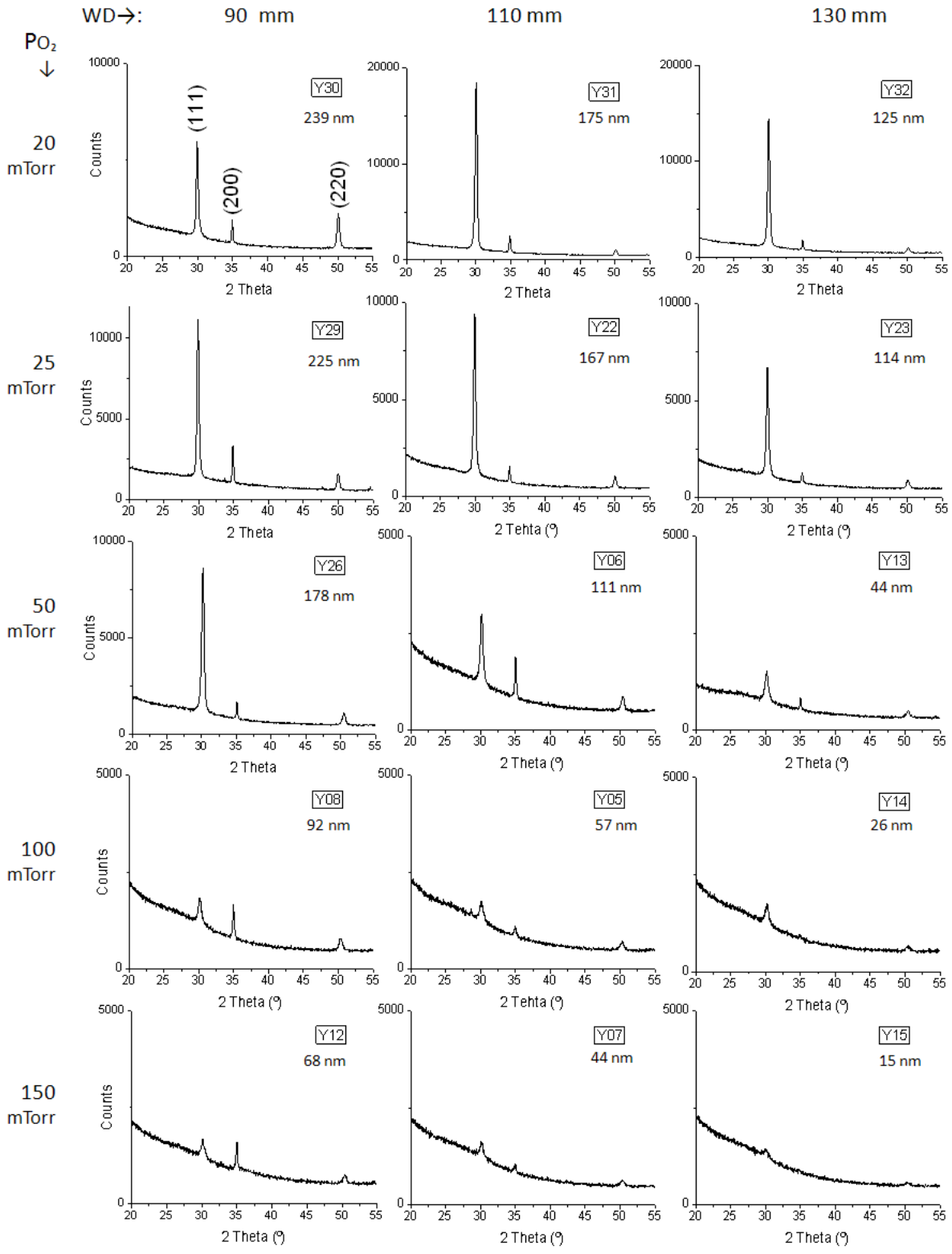

Figure 20: *XRD diffraction pattern as a function of P_{O_2} and WD, i.e. pressure increases along the y-axis, and the working distance along the x-axis. The YSZ film-thickness is indicated for convenience.*

3.3 SEM-results

3.3.1 Planar view

In Fig. 21 one can observe the planar view of samples deposited under different conditions. The WD is indicated on the top, while the pressure is indicated to the left. The magnification is 100 000 in every image (the reader is asked to ignore the magnification appearing in the SEM-images, but rather use the scale-bars as a reference).

All the samples deposited at 20 and 25 mTorr appear dense. Columns (elongated grains) are distinguishable, but there does not seem to be any major topographical differences. The density of the samples deposited at 50, 100 and 150 mTorr appears to decrease with decreasing WD. Sample Y26 and Y08 (deposited at 90 mm WD and 50 and 100 mTorr, respectively) appear very porous, with very distinguishable pores (black areas) and elongated grains (white areas).

The density of the samples deposited at 20 and 25 mTorr observed in Fig. 21 combined with the preferred (111) orientation in these samples presented in Fig. 20, is ascribed to the high kinetic energy of the condensed atoms in the substrate surface. Assuming that at the nucleation stage, the density of grains with various orientation was almost the same for all depositions (as the thermal energy was the same in each deposit), the density of these samples of high orientation implies that the mobility of the surface atoms and adatmos is sufficient to "convert" neighboring grains of non-preferred orientation into a grain of the energetically favored (111) orientation (lower interface energy with the substrate), and in that way combine preferential growth with density.

In sample Y26 and Y08 (deposited at 90 mm WD and 50 and 100 mTorr, respectively), the pores are assumed to represent hollow channels residing from shadowing effects imposed by neighboring, faster growing grains. This assumption is based on the XRD patterns corresponding to sample Y26 and Y08 in Fig. 20, where sample Y08 showed a tendency towards a (200) orientation, and sample Y26 show a clear (111) orientation. Both samples appear porous because at 50 and 100 mTorr, the kinetic energy of the ablated species is sufficiently reduced, and preferential growth is associated with shadowing effects of neighboring grains of non-preferred orientation. At 50 mTorr and 90 WD (sample Y26), the mobility of the surface atoms seems to be sufficient for diffusions of adatoms to the preferred (111)-oriented grains, but insufficient to convert neighboring grains of another orientation, which is why shadowing effects lead to high porosity.

The same columnar pores appear to be present in sample Y06 and Y13 (deposited at 50 mTorr) and sample Y05 and Y14 (deposited at 100 mTorr), but they seem smaller, which is expected for thinner layers, where the shadowing effect is less developed.

Sample Y12 (150 mTorr) also seems porous, while sample Y07 and Y15 seems perfectly dense. This appearance is attributed to their YSZ film thickness of 44 and 15 nm, respectively, based on reasons mention above. The particles observed in samples Y29, Y22 and Y23 will be discussed in a later section.

3.3.2 Cross sectional view

The YSZ layers were identified on all samples, indicated with red arrows in Fig. 22. A clear tendency towards densification of the columnar structure with decreasing pressure can be detected by examine sample Y08, Y26, Y29 and Y30 (90 mm WD). In sample Y26 (and Y08)

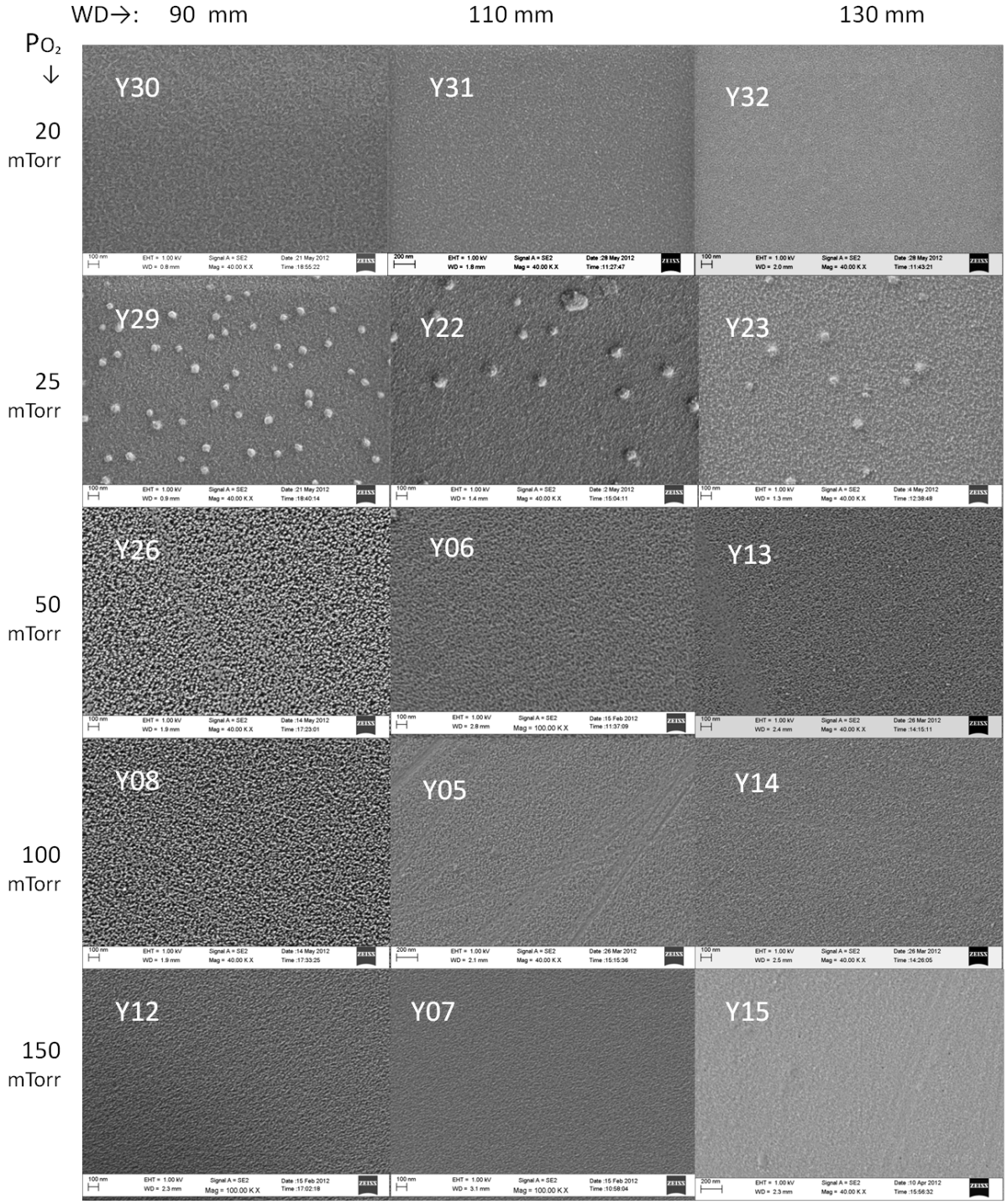

Figure 21: *SEM images from the samples constituting the matrix. The magnification is 100 000 in all images. The reader is asked to consequently use the scale-bars as a reference, and not the numeric value of magnification on samples Y13-Y34)*

black columns correspond to porous columns that were observed as pores in the planar SEM image in Fig. 21.

Many of the columns appear to span the whole film-thickness in the samples deposited at

20 mTorr, this is best detected by observing sample Y30 in Fig. 22.

A developed columnar structure is not observed for sample deposited at 150 mTorr, nor for sampled deposited at a WD of 130 mm and a P_{O_2} of 100 and 50 mTorr. This is probably due to the modest film-thickness of these layers.

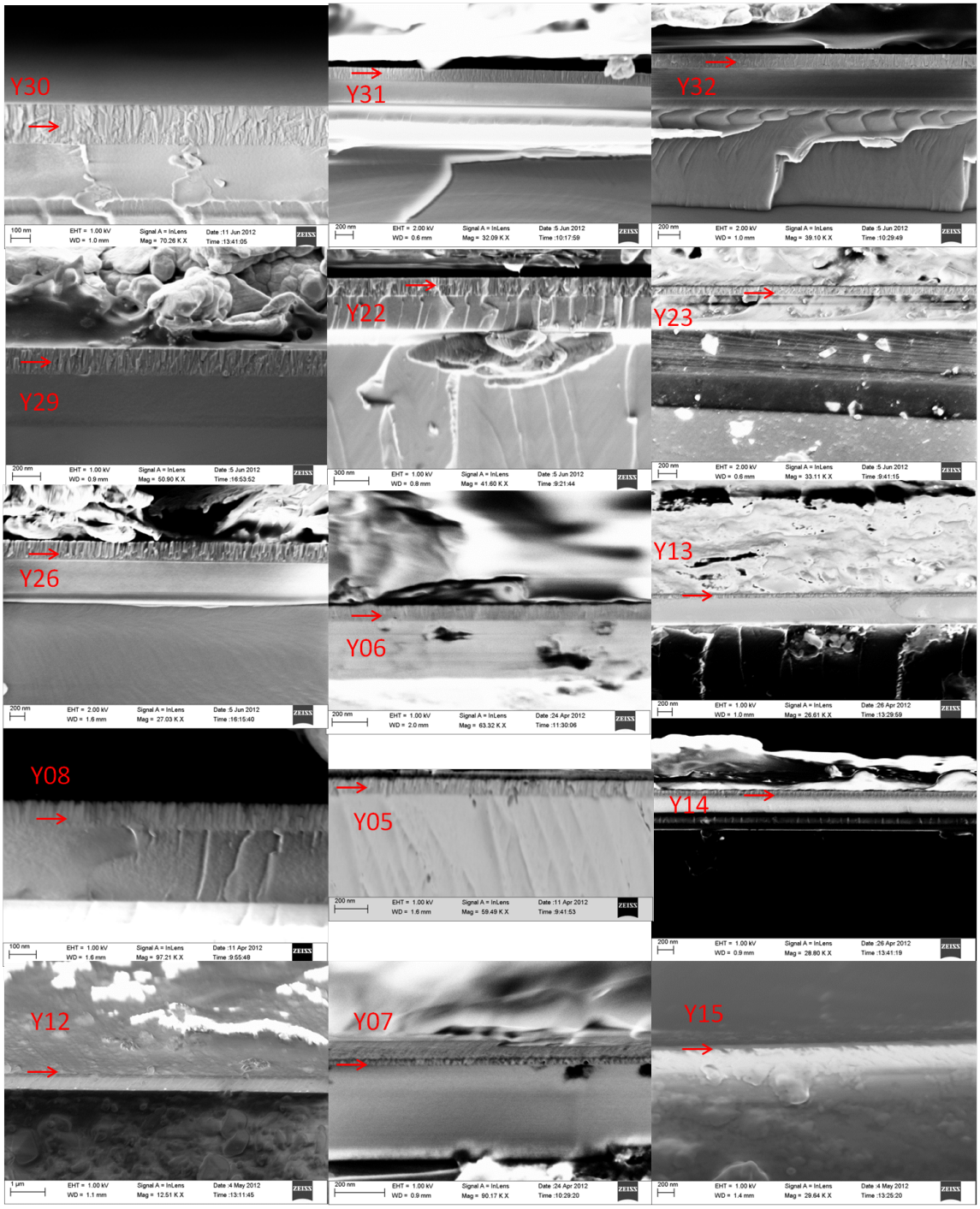

Figure 22: *SEM cross sectional images. The YSZ layer on each sample is indicated with red arrows. Other features in the images are either silver paste or the substrate material.*

3.4 Comparison of XRD and SEM results

To facilitate observations of the tendency of changes in the microstructure with decreasing pressure, sample Y25 and Y28, deposited at 35 and 30 mTorr, respectively, are included in Fig. 23, which show the planar SEM, XRD pattern and cross sectional SEM results all together for six samples deposited at 90 mm WD with different P_{O_2}.

Densification of the structure is clearly observed with decreasing pressure both in planar and cross sectional SEM images, as stated previously. A threshold value for achieving dense films seems to be reached between 50 and 35 mTorr, see sample Y26 and Y25 in Fig. 23. This is in good accordance with Infortuna et al. that reported a similar threshold value of 37 mTorr when depositing YSZ at 400°C [4].

The tendency in the XRD patterns (from higher to lower pressure) is the same as for the tendencies previously observed. A "maximum" for (111) orientation appears to be reached at 35 mTorr (sample Y25), while the tendency towards bulk-8YSZ microstructure begins below 35 mTorr, see the XRD patterns of sample Y28, Y29 and Y30 in Fig. 23.

To minimize the effect of film thickness, Fig. 24 presents the XRD results in Fig. 23 with the peak intensities normalized with respect to film thickness. This was done by multiplying the counts from the XRD results with a factor, F. The factor F was the reciprocal of a samples film thickness, T_s divided by the film thickness of the thickest sample T_{Y30} (239 nm), i.e. $F = 1/(T_s/T_{Y30})$.

The rather extreme (111) orientation of sample Y25 becomes very clear when compared with the other samples in Fig. 24. Also, a resemblance of the XRD pattern of sample Y26, Y28 and Y29 is detected. Similar XRD patterns in this figure implies that the film is composed of more or less the same relative amounts of grains with a given orientation. SEM planar images in Fig. 23 gives however little doubt that sample Y28 and Y29 are much denser than sample Y26, even if they have show the same preferred (111) orientation. This support the previous theory that the pronounced (111)-orientation of samples deposited below 50 mTorr is due to the conversion of neighboring grains, while at 50 mTorr and above, preferred orientation (both (111) or (200)) is associated with faster growing grains and subsequent shadowing effects.

The particulates appearing in sample Y28 and Y29 will be discussed in a later section.

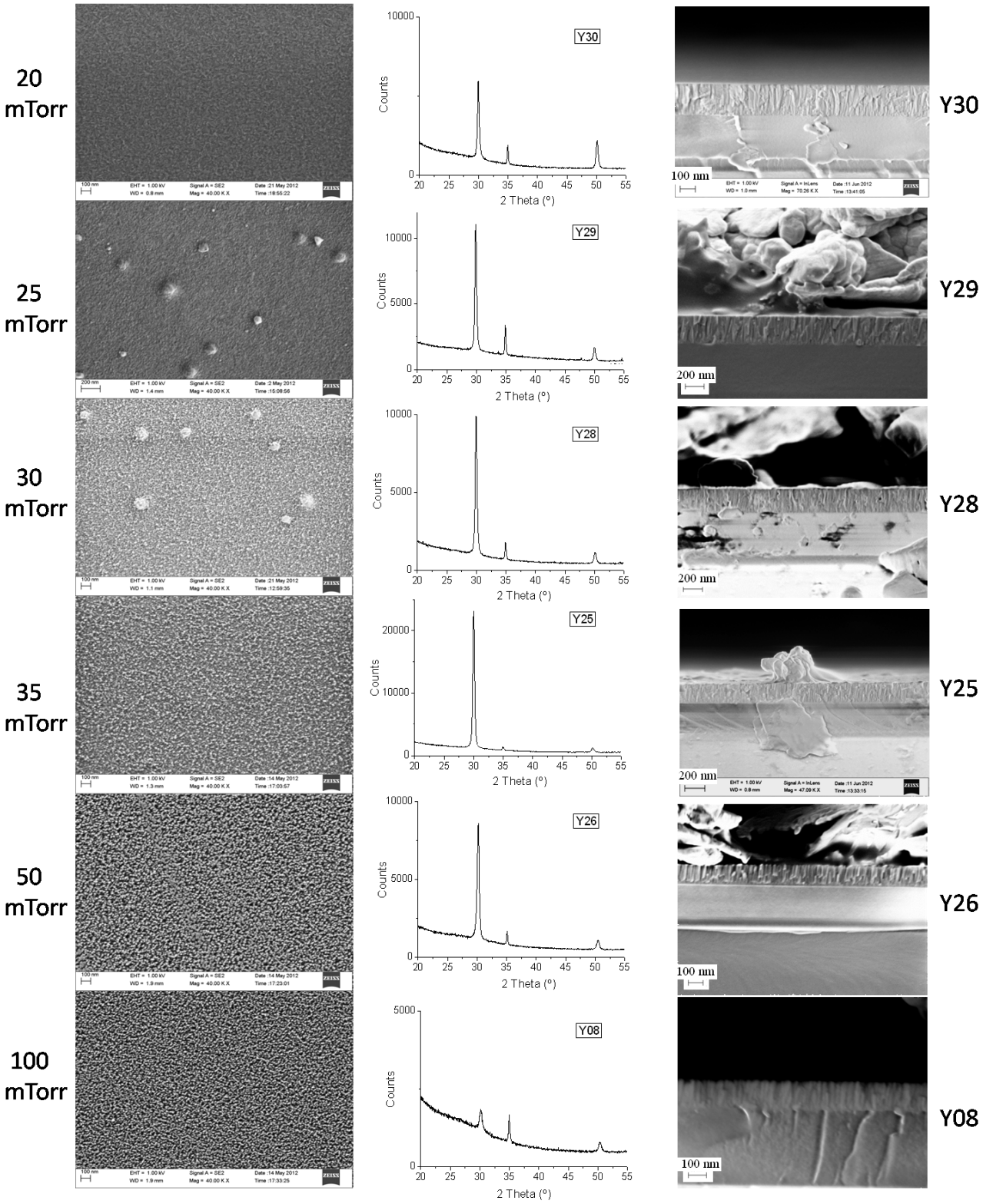

Figure 23: *Planar SEM, XRD and cross sectional SEM images of six samples deposited with a WD of 90 mm and different P_{O_2}. Each image in the same line represents the same sample, and the sample name is indicated to the far right and in the XRD patterns. The deposition pressure is indicated to the left.*

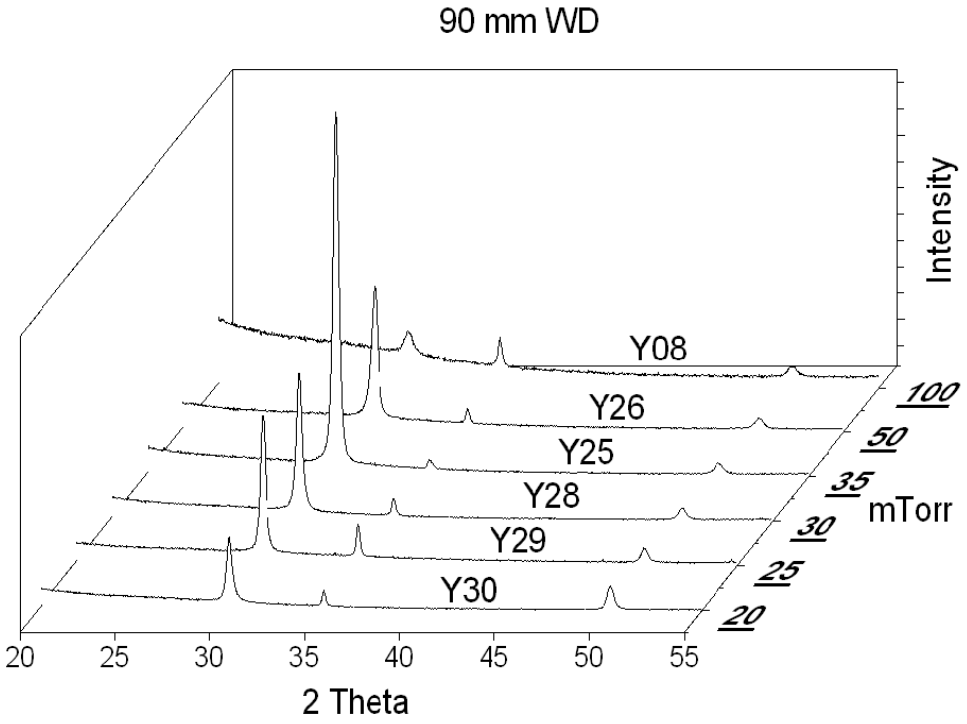

Figure 24: *Normalized XRD patterns for samples deposited at 90 mm WD.*

3.5 Influence of film thickness on XRD and microstructure

As the tendency of preferred orientation from the previous section has a possible bias residing from film-thickness, it is interesting observe the results presented in Fig. 25. The two samples presented were deposited under the same conditions (100 mTorr and a WD of 90 mm), but differ in thickness, as Y33 was deposited with twice as many laser pulses as Y08. Sample Y08 has a slight tendency towards a (200) orientation, see Fig. 25a, while sample Y33 has pronounced and clear (200) orientation, see Fig. 25d. As already discussed, it is presumed the film growth at 100 mTorr proceeded without any significant influence of surface diffusion (due to lower kinetic energy of the species). The faster growing (200) oriented grains will then gradually dominate more and more with increasing film thickness, and this phenomenon is clearly observed in Fig. 25a and 25d. The planar SEM images in Fig. 25b and 25e also supports this theory, as the black areas in sample Y33 appears larger due to a more porous structure, as the shadowing effect develops with film thickness. Porous channels are observed in both samples, but are more pronounced in sample Y33, see Fig. 25c and 25f, also supporting the theory proposed both here and by Xiong Xuming et al. in reference [27], as mentioned above.

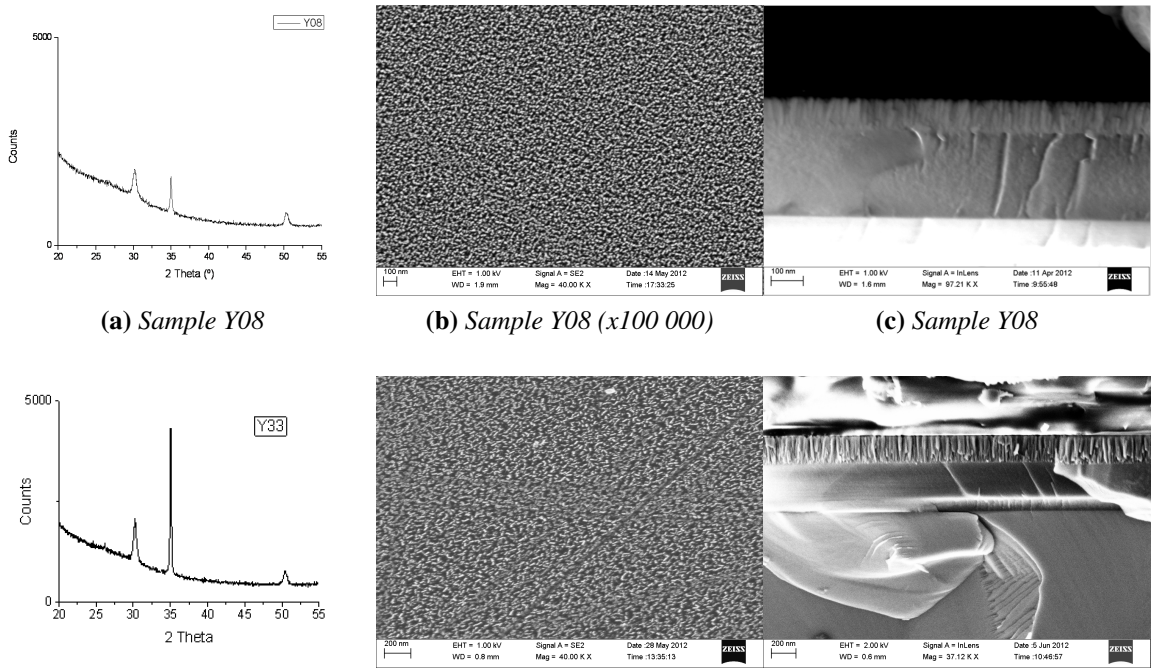

(a) *Sample Y08* **(b)** *Sample Y08 (x100 000)* **(c)** *Sample Y08*

(d) *Sample Y33* **(e)** *Sample Y33 (x100 000)* **(f)** *Sample Y33*

Figure 25: *SEM images and XRD diffraction pattern of sample Y08 and Y33. Both samples have a YSZ layer deposited with the same parameters, but differ in total amount of laser pulses and hence thickness. The YSZ layer on sample Y08 and Y33 are 92 and 205 nm, respectively.*

3.6 TEM analysis

TEM images of sample Y29 are shown in Fig. 26. Crystalline, elongated grains are outlined with white lines in Fig. 26 i), ii) and iii). The film appears dense, with no visible voids between the columns. This supports and underlines the previous observations made, that a dense, crystalline, columnar structure develops when depositing at low deposition pressures.

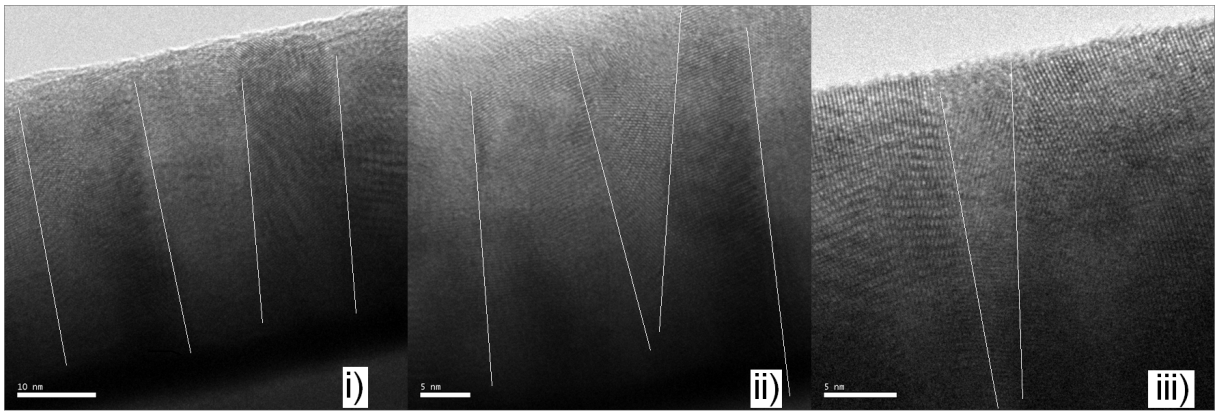

Figure 26: *TEM images of sample Y29. The magnification is 250 000, 330 000 and 480 000 in i), ii) and iii), respectively. The white lines indicate the grain boundaries.*

3.7 Particle ejection

Particles were observed in all samples, examples are given in Fig. 27. Fragments from the target have been ejected during deposition and caused inhomogeneities and pinholes. Based on this observation it would be beneficial to change from 8YSZ to plasma spark sintered 3YSZ, which have superior mechanical properties, reported by I. Garbayo et al. in reference [1].

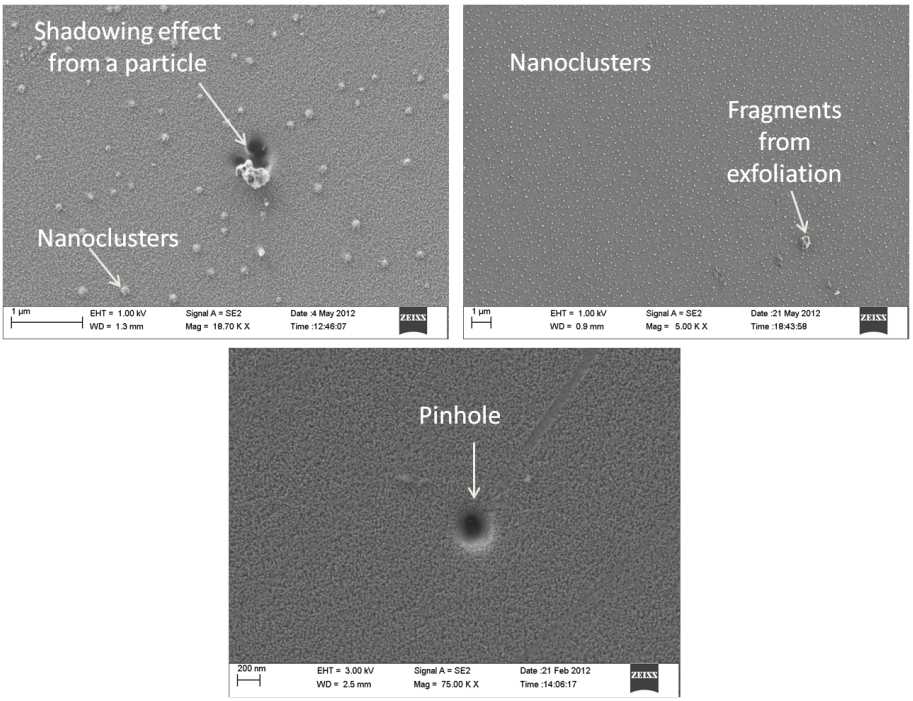

Figure 27: *Ejected particles and pinholes*

Spherical nanoclusters, observed only on samples deposited at 25 and 30 mTorr, are presented in Fig. 28a and 28b. From theory it is known that such nanoclusters origin from particle saturations in the plume, as the plume expansion is limited by the presence of gas molecules. The number of nanoclusters appears to decrease with increasing WD, see Fig. 28a and with increasing pressure, see sample Y28, Fig. 28b. This can be explained by considering that the nanoclusters scatter upon collision with oxygen molecules, and a longer travel distance, or a higher number of oxygen molecules (higher pressure) therefor implies that less nanoclusters arrive to the substrate surface.

The lack of such nanoclusters in samples depositede at 20 mTorr might imply that the plume expands sufficiently, avoiding a critical saturation of particles and hence cluster-nucleation at this pressure, or that the clusters arrive at the substrate surface with sufficient energy to dissociate.

The nanoclusters do not appear to exert any shadowing effect, and in sample Y23 in Fig. 21 it appears like the clusters are "berried" in new, incoming particles that nucleate and grow on top of the nanocluster.

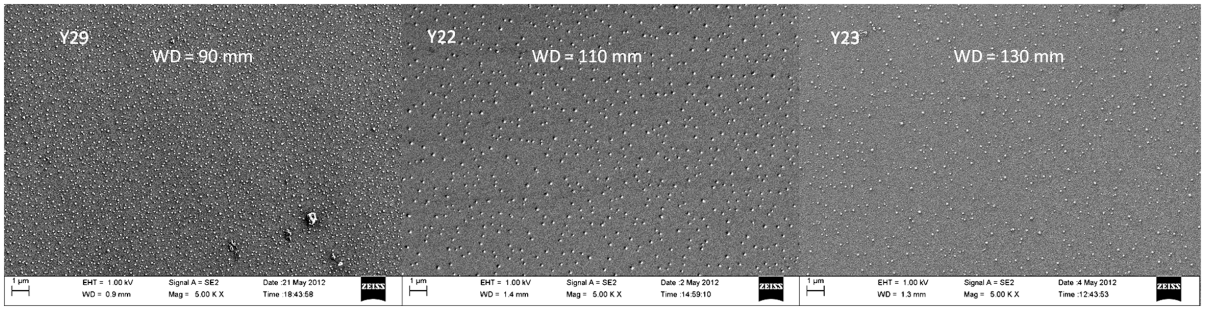

(a) *Nanoclusters in sample Y29, Y22 and Y23 (25 mTorr)*

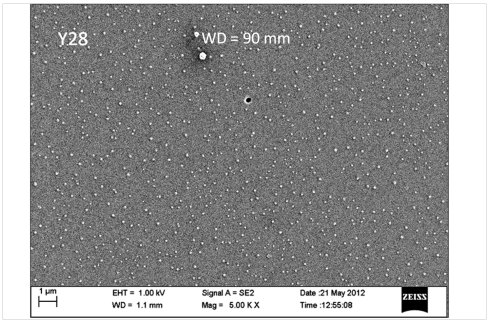

(b) *Nanoclusters in sample Y28 (30 mTorr)*

Figure 28: *Nanoclusters observed in samples deposited at 25 and 30 mTorr. Sample Y29 and Y28 are deposited at a WD of 90 mm, while Y22 and Y23 at a WD of 110 and 130 mm, respectively.*

3.8 Deposition of YSZ on 4 inch wafers

The film thickness profile and visual appearance of the four wafers deposited with YSZ can be observed in Fig. 29. The thickness varies from the border of the wafers toward the center on all wafers, with the highest standard deviation (STD) in wafer 1, see Fig. 29a. Wafer 2 has an improved homogeneity, with a STD of 9 nm. However, the YSZ thickness is small, ranging between 50 and 75 nm approximately, and it is assumed that a less homogeneous profile will develop with increasing film thickness. Wafer 3 and 4 have both increased film thickness compared to wafer 2, and increased homogeneity compares to wafer 1. This can also be observed visually when comparing wafer 1 to wafer 4, as the blue area in Fig. 29e is bigger than the blue area in Fig. 29b (indicating a larger homogeneous area in wafer 4). The lower pressures applied during deposition of wafer 3 and 4 is the reason for the superior thickness, while a more optimized rastering improves homogeneity. Wafer 3 has a rastering velocity 750 times faster in the middle of the target than at the target extreme, and the plume was never positioned under the center of the wafer, and explains why a decrease in thickness is observed in the center of the wafer. Wafer 4 has a velocity 375 times greater at 2/3 of the target diameter (just below the center of the wafer) than in the target extreme. This might appear to be too slow, because the film thickness is about 50 nm thicker in the center than in the extremes.

In all wafers, the extremes have a significantly reduced film thickness compared to the more homogeneous central areas. This effect can, to some extent, also be ascribed to the shadowing effect exerted by the PLD sample holder.

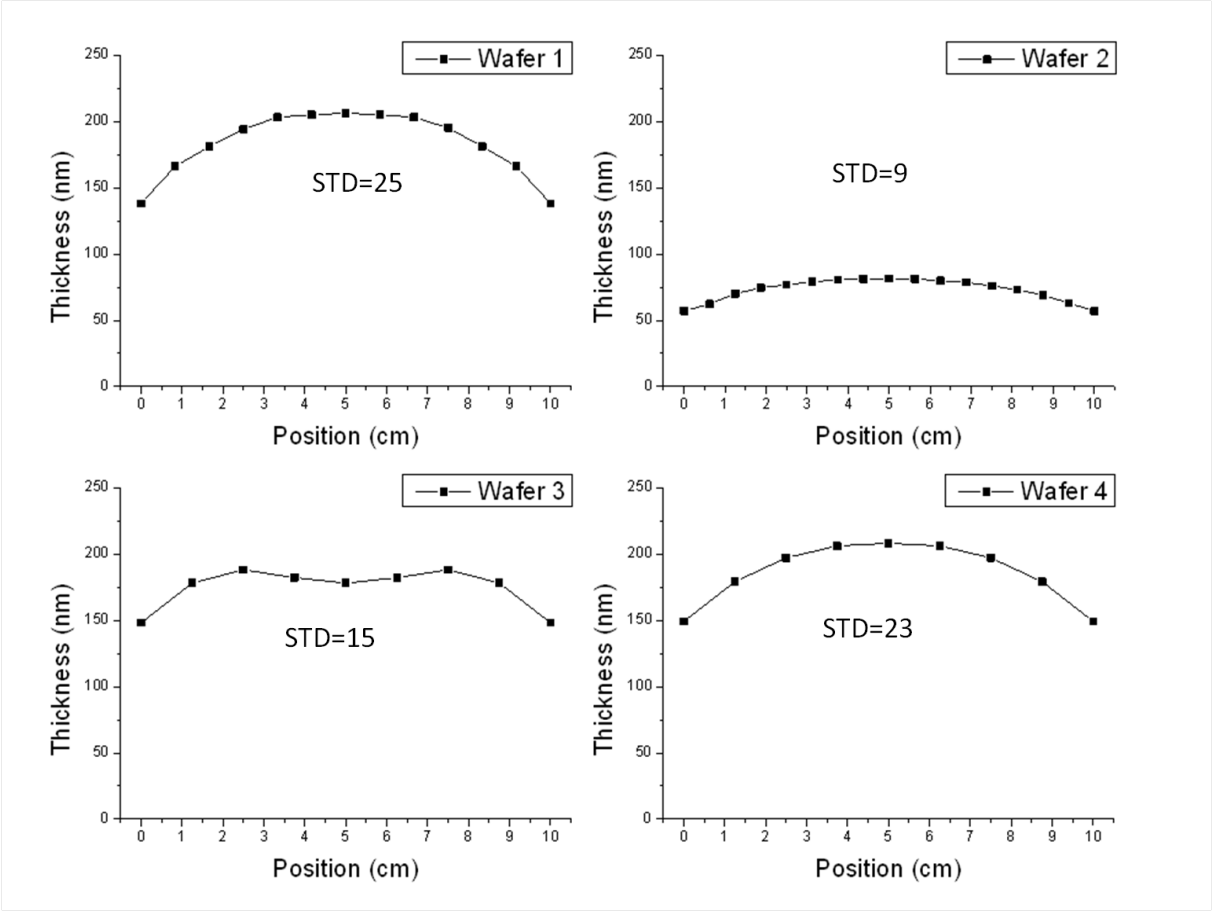

(a) *Thickness profile of the YSZ-layer on wafer 1-4. The STD is indicated in each graph*

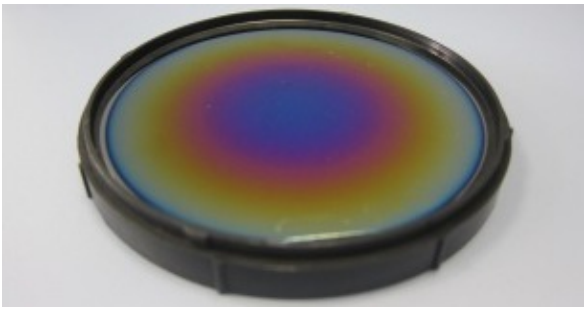

(b) *Wafer 1. YSZ on silicon substrate*

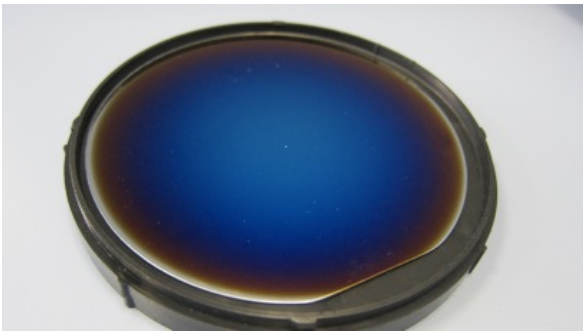

(c) *Wafer 2. YSZ on silicon substrate*

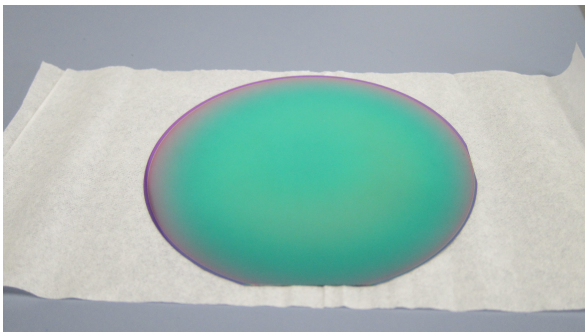

(d) *Wafer 3. YSZ on multilayer Si/SiO/Si_3N_4 substrate*

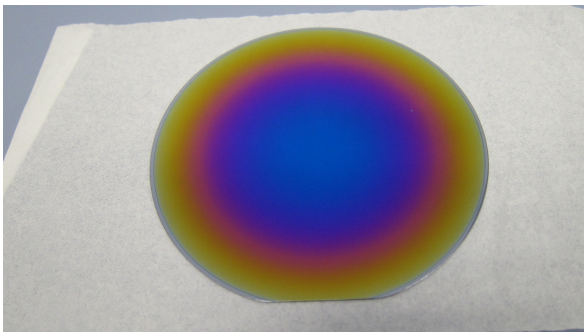

(e) *Wafer 4. YSZ on silicon substrate*

Figure 29: *Thickness profile of the YSZ-layer and photos of wafer 1-4*

4 Conclusions

It has been found that the thickness and microstructure of 8YSZ thin-films deposited by the PLD technique onto amorphous Si-based substrates holding a temperature of 600°C show a great dependency on background pressure, P_{O_2} and target-substrate distance (WD).

The film thickness obtained ranged from 15 to 239 nm, and was found to increase exponentially with decreasing pressure, and linearly with decreasing WD. This is due to the decrease in collisions and scattering of ablated material with both decreasing pressure and WD. It was found that above 50 mTorr, the plume expansion is limited to below the minimum WD of 90 mm, resulting in very low deposition rates.

The microstructure show a great variation with the deposition background pressure, P_{O_2}. Between 50 and 35 mTorr, a tendency towards densification of the deposited films have been observed, while samples deposited at 25 and 20 mTorr appear fully dense. This is in accordance with experimental results reported by Infortuna et al. which identified a threshold value of 37 mTorr when depositing YSZ at 400°C [4]. This threshold value can be interpreted as the maximum pressure applicable to remain in the zone 2 in Thornton's structure zone model when depositing YSZ at a substrate temperature of 600°C.

The increased density in the deposited films at lower pressures was due to higher mobility of the ablated species at the substrate surface, as the kinetic energy is conserved to a higher degree. A higher mobility allows for significant surface diffusion and rearrangement of the grain orientation into the energetically favored (111) orientation, which was clearly observed in the XRD analysis for samples deposited below 50 mTorr. The driving force of this phenomenon is the reduction in free energy of the system, as the interface energy between the amorphous substrate and the high density (111) plane of YSZ is the lowest available.

A tendency of preferred growth of the (200) oriented grains was identified above 50 mTorr, and was more pronounced in thicker films. The (200) orientation was associated with insignificant surface diffusion, as faster growing (200) oriented grains do not lose atoms by diffusion to lower energy (111) oriented grains if the mobility of the atoms is insufficient. The high porosity in samples deposited above 50 mTorr came from the shadowing effect the faster growing (200) oriented grains exerted on neighboring grains, and developed with increasing film thickness. Elongated pores representing hollow columns were identified in sample deposited at 50 mTorr and higher, supporting this theory. The phenomenon that the (200) orientation gradually dominates with increasing film thickness when mobility of the species at the substrate surface is reduced is also reported by Xiong Xuming et al. in reference [27].

A tendency towards developing a microstructure similar to that of bulk 8YSZ was observed for the thickest films, which is due to growth instability and a tendency towards formation of new grains with an increasing film thickness. As the grain orientation is no longer effected by the interface energy between the grain and the substrate, a grain-orientation distribution similar to that of bulk-YSZ is formed. This tendency was first observed in samples deposited at 30 mTorr (WD of 90 mm), where the sample thickness was 202 nm.

The WD was found to have little influence on the grain orientation (i.e. the kinetic energy of the condensed species) below 50 mTorr, and mainly influenced the film thickness, as an increased WD is associated with a lower deposition rates.

Particles and fragments from the target were identified on all samples. Improving the mechanical properties of the target is expected to decrease the number of particles, as reported by I. Garbayo et al. in reference [1]. Nanoclusters residing from the plume were identified on

samples deposited at 25 and 30 mTorr exclusively, but did not appear to exert any shadowing effects. At 20 mTorr these clusters are assumed to have sufficient kinetic and thermal energy to dissociate, while above 30 mTorr, they scatter before they can reach the substrate surface, which explain why such nanoclusters were not observed for any other deposition pressure.

Based on the findings here highlighted, the PLD deposition conditions for achieving a dense and crystalline YSZ thin-film of columnar grains at a deposition temperature of 600°C, with a reasonable deposition rate and without the presence of nanoclusters, is a P_{O_2} of 20 mTorr and a WD of 90 mm. Depositing under these conditions yields a YSZ thin-film which meets the requirements for micro-SOFC electrolyte applications.

For deposition of larger wafers, film thickness homogeneity improved by performing a very slow rastering in the extreme of the target, while moving faster towards the center. To further optimize mirror rastering, it is recommendable to resort to computer programming, to simulate the movement of the plume across the rotating wafer and predict the required velocities in given intervals.

References

[1] I.Garbayo, G.Dezanneau, C.Bogicevic, J.Santisi, I.Grácia, N. Sabaté, and A. Tarancon. Pinhole-free ysz self-supported membranes for micro solid oxide fuel cell applications. *Solide State Ionics*, 2011.

[2] A.Evans, Anja Bieberle-Hutter, Jennifer L.M Rupp, and Ludwig J. Gauckler. Review on microfabricated micro-solid oxide fuel cell membranes. *Journal of Power Sources*, 2009.

[3] Antti Hakola. Laser ablation and thin-film deposition. Master's thesis, Helsinki University of Technology, 2011.

[4] A. Infortuna et al. Microstructure of cgo and ysz thin films. *Advanced Functional Materials*, 18:127–135, 2008.

[5] Hans-Ulrich Krebs, Martin Weisheit, Jörg Faupel, Erik Süske, Thorsten Scharf, Christian Fuhse, Michael Störmer, Kai Sturm, Michael Seibt, Harald Kijewski, Dorit Nelke, Elena Panchenko, and Michael Buback. Pulsed laser deposition (pld) - a versatile thin film technique. *Advanced Solid State Physics*, 43:505–517, 2003.

[6] Jim Greer. *Chapter 9: Large -Area Commercial Pulsed Laser Deposition*. John Wiley &Sons, Inc., 2007.

[7] Robert J. Kee, Huayang Zhu, A. Mary Sukeshini, and Gregory S. Jackson. Solid oxide fuel cells: Operating principles, current challenges, and the role of syngas. *Combustion Science and Technology*, 180:1207–1244, 2008.

[8] Y.D Premchand, A. Bieberle-Hütter, and L.J. Gauckler. Fuel cells-solid oxide fuel cells / micro cells. *Encyclopedia of Electrochemical Power Sources*, pages 148–157, 2009.

[9] Smithsonian Institution. *http://americanhistory.si.edu/fuelcells/basics.htm*. National Museum of American History, 2008.

[10] I. Garbayo, A. Tarancón, J. Santiso, F. Peiró, E. Alarcón-LLadó, A. Cavallaro, I. Gràcia, C. Cané, and Neus Sabaté. Electrical characterization of thermomechanically stable ysz membranes for micro solid oxide fuel cells applications. *Solid State Ionics*, 181:322–331, 2010.

[11] J. Fleig, H.L Tuller, and J. Maier. Electrodes and electrolytes in micro-sofcs: A discussion of geometrical constraints. *Solid State Ionics*, 174:261–270, 2004.

[12] Samuel Rey-Mermet. *Microfabricated Solid Oxide Fuel Cells*. PhD thesis, Ecole Polytechnique federale de Lausanne, 2008.

[13] Masaru Tsuchiya, Bo-Kuai Lai, and Shriram Ramanthan. Scalable nanostructured membranes for solid-oxide fuel cells. *Nature nanotechnology*, 2011.

[14] Babak Ziaie, Antonio Baldi, and Massood Z. Atashbar. Nanostructures, micro/nano fabrication, and micro/nanodevices. *Springer handbook of nanotechnology*, pages 147–202, 2004.

[15] Albert Tarancon, Neus Sabaté, Andrea Cavallaro, Isabel Gràcia, Jaume Roqueta, Iñigo Garbayo, Juan P. Esquivel, Gemma Garcia, Charles Cane, and José Santiso. Residual stress of free standing membranes of yttria-stabilized zirconia for micro solid oxide fuel cell applications. *Journal of Nanoscience and nanotechnology*, 10:1–11, 2010.

[16] Erich Kisi. *Zirconia Engineering Ceramics, Old Challanges-New Ideas*. Trans Tech Publications, 1998.

[17] Paul Inge Dahl. *Synthesis and characterization of ionic conductors based on ZrO2, BaZrO3 and SrCeO3 and Preparation of LaFeO3 and LaCoO3 thin films*. PhD thesis, Norwegien University of Science and Technology, 2006.

[18] H. Hidalgoa, E. Reguzinaa, E. Millona, A.-L. Thomanna, J. Mathiasa, C. Boulmer-Leborgnea, T. Sauvageb, and P. Brault. Yttria-stabilized zirconia thin films deposited by pulsed-laser deposition and magnetron sputtering. *Surface and Coatings Technology*, 205:4495–4499, 2011.

[19] Anil V. Virkar. Sofc materials and processing issues. 2001.

[20] Cambridge university. *www.doitpoms.ac.uk/tlplib/fuel-cells/index.php*.

[21] Sebastian Heiroth, Ruggero Frison, Jennifer L.M. Rupp, Thomas Lippert, Eszter J. Barthazy Meier, Elisabeth Müller Gubler, Max Döbeli, Kazimierz Conder, Alexander Wokaun, and Ludwig J. Gauckler. Crystallization and grain growth characteristics of yttria-stabilized zirconia thin films grown by pulsed laser deposition. *Solid State Ionics*, 191:12–23, 2011.

[22] Jennifer L.M Rupp. Ionic diffusion as a matter of lattice-strain for elctroceramic thin films. *Solid State Ionics*, 207:1–13, 2012.

[23] Pulsed laser deposition (pld) of thin films.

[24] I. Petrov, P.B. Barna, L.Hultman, and J.E.Green. Microstructural evolution during film growth. *Journal of Vaccum Science Technology*, 5:117, 2003.

[25] Micheal N.R Ashfold, Fredrik Claeyssens, Garth M. Fuge, and Simon J. Henley. Pulsed laser ablation and deposition of thin films. *School of Chemistry, University of Bristol, Bristol, UK*, 2003.

[26] E. G. Gamaly, N. R. Madsen, M. Duering, A. V. Rode, V. Z. Kolev, and B. Luther-Davies. Ablation of metals with picosecond laser pulses: Evidence of long-lived nonequilibrium conditions at the surface. *Physical Review*, 71, 2005.

[27] Xuming Xiong, Yueliang Zhou, Zhenghao Chen, Huibin Lü, Aijun Zhu, Dafu Cui, Huisheng Wang, and Guozhen Yang. Room temperature deposition of yttria-stabilized zirconia buffer layer on metallic substrates by laser ablation. *Chinese Science Bulletin*, 42:1345–1350, 1997.

[28] Carl V. Thompson. Grain growth in thin-films. *Annu. Rev. Mater. Sci.*, 20:245–268, 1990.

[29] PANalytical software database. 8ysz bulk xrd reference pattern.

[30] A. Mazor, D.J Srlolovitz, P.S Hagan, and B.G. Bukiet. Columnar growth in thin films. *Physical Review Letters*, 60:424–427, 1988.

[31] Laser machining processes: Chapter 2: Laser basics. *Columbia University*.

[32] Dr. Rüdiger Paschotta. Encyclopedia of laser physics and technology. *RP photonics*, 2010.

[33] F. sanchez, R. Aguiar, P. Serra, M. Varela, and J.L Morenza. Study of material emission in arf and krf excimer laser ablation of yttria stabilized zirconia single crystals. *Thin Solid Films*, 317:108–111, 1998.

[34] Coherent. User manual compex pro 205. *Laser User Manual*, 2008.